

# CHARGE AND SPIN TRANSPORT OF METAL/FERROMAGNET JUNCTIONS



Krisakron Pasanai

A Thesis Submitted in Partial Fulfillment of the Requirements for the

Degree of Doctor of Philosophy of Science in Physics

Suranaree University of Technology

Academic Year 2010

การขนส่งประจุและสปีนของรอยต่อระหว่าง  
โลหะ/สารเฟอร์โรแมกเนต



วิทยานิพนธ์นี้เป็นส่วนหนึ่งของการศึกษาตามหลักสูตรปริญญาวิทยาศาสตรดุษฎีบัณฑิต  
สาขาวิชาฟิสิกส์  
มหาวิทยาลัยเทคโนโลยีสุรนารี  
ปีการศึกษา 2553

# CHARGE AND SPIN TRANSPORT OF METAL/FERROMAGNET JUNCTIONS

Suranaree University of Technology has approved this thesis submitted in partial fulfillment of the requirements for the Degree of Doctor of Philosophy.

Thesis Examining Committee

---

(Asst. Prof. Dr. Chinorat Kobdaj)

Chairperson

---

(Assoc. Prof. Dr. Puangratana Pairor)

Member (Thesis Advisor)

---

(Assoc. Prof. Dr. Udomsilp Pinsook)

Member

---

(Assoc. Prof. Dr. Prapun Manyum)

Member

---

(Dr. Michael F. Smith)

Member

---

(Prof. Dr. Sukit Limpijumnong)

Vice Rector for Academic Affairs

---

(Assoc. Prof. Dr. Prapun Manyum)

Dean of Institute of Science

กฤษกร ปาสาโน : การขนส่งประจุและสปินของรอยต่อระหว่างโลหะ/สารเฟอร์โรแมกเนต (CHARGE AND SPIN TRANSPORT OF METAL/FERROMAGNET JUNCTIONS) อาจารย์ที่ปรึกษา: รองศาสตราจารย์ ดร. พวงรัตน์ ไพเราะ, 70 หน้า.

วิทยานิพนธ์นี้เป็นการศึกษาเชิงทฤษฎีเกี่ยวกับสเปกโทรสโกปีการทะลุผ่านในรอยต่อระหว่างโลหะและเฟอร์โรแมกเนตโดยการใช้วิธีการกระเจิงแบบเมตริก ในการประมาณแบบหนึ่งแถบพลังงาน พบว่า ในสเปกตรัมความนำไฟฟ้าความชันมีการเปลี่ยนแปลงตรงกับจุดต่ำสุดของแถบพลังงานรองในสารเฟอร์โรแมกเนต ในกรณีที่ไม่มีการกระเจิงที่ทำให้สปินเปลี่ยนทิศทาง พบว่า การกระเจิงปกติค่าสปินไม่มีการเปลี่ยนแปลงทำให้ค่าสภาพความนำไฟฟ้ามีค่าลดลง แต่เมื่อมีการกระเจิงที่ทำให้สปินเปลี่ยนทิศทาง สภาพความนำไฟฟ้าในรอยต่อที่มีการกระเจิงปกติสูงสามารถมีค่าเพิ่มขึ้นได้จนมีค่าสูงสุด สำหรับค่าสปินโพลาริเซชันของกระแสในรอยต่อที่มีการกระเจิงแบบปกติต่ำจะมีค่าเพิ่มขึ้นตามค่าการกระเจิงที่ทำให้สปินเปลี่ยนทิศทาง ในรอยต่อที่มีการกระเจิงปกติสูงสปินโพลาริเซชันของกระแสในระบบรอยต่อหนึ่งมิติขึ้นกับการกระเจิงที่ทำให้สปินเปลี่ยนทิศทางน้อย แต่ในทางตรงกันข้ามสปินโพลาริเซชันของกระแสในระบบรอยต่อสองและสามมิติที่มีการกระเจิงปกติสูงมีค่าเพิ่มขึ้นตามค่าการกระเจิงที่ทำให้สปินเปลี่ยนทิศทางจนมีค่าสูงสุดซึ่งมีค่ามากกว่าค่าสูงสุดในรอยต่อที่มีการกระเจิงปกติต่ำ ในการประมาณแบบสองแถบพลังงาน การกระเจิงที่ทำให้สปินเปลี่ยนไม่ถูกนำมาพิจารณา การคำนวณจะพิจารณาการควบคู่ของแถบพลังงานแบบเอสและแบบดี พบว่า เมื่อการควบคู่นี้เป็นศูนย์สเปกตรัมพลังงานจะเกิดการตัดกันหลายจุด แต่เมื่อควบคู่ไม่เป็นศูนย์เกิดช่องว่างพลังงานขึ้นที่บริเวณจุดตัดของสเปกตรัมพลังงานที่มีสปินเหมือนกัน โดยขนาดของช่องว่างแถบพลังงานจะขึ้นอยู่กับค่าความแรงการควบคู่ นอกจากนี้ จะเกิดรอยหักตรงบริเวณจุดตัดดังกล่าวในความหนาแน่นสถานะ รอยหักนี้จะส่งผลต่อสมบัติอื่นๆ ในรอยต่อ สภาพนำไฟฟ้าในรอยต่อมีค่าสูงสุดเมื่อมวลยังผลของอิเล็กตรอนในโลหะมีค่าใกล้เคียงกับมวลยังผลของอิเล็กตรอนของแถบพลังงานหลักของวัสดุเฟอร์โรแมกเนต

สาขาวิชาฟิสิกส์  
ปีการศึกษา 2553

ลายมือชื่อนักศึกษา \_\_\_\_\_  
ลายมือชื่ออาจารย์ที่ปรึกษา \_\_\_\_\_

KRISAKRON PASANAI : CHARGE AND SPIN TRANSPORT OF  
METAL/FERROMAGNET JUNCTIONS. THESIS ADVISOR :  
ASSOC. PROF. PUANGRATANA PAIROR, Ph.D. 70 PP.

## CHARGE AND SPIN TRANSPORT/ FERROMAGNET

The tunneling spectroscopy of a metal/ferromagnet junction are theoretically studied using a scattering matrix approach. In one-band model, there is a change in slope of the conductance spectrum at the energy equivalent to the bottom of the minority band. In the absence of interfacial spin-flip scattering, the normal scattering always suppress the conductance spectrum. But when the spin-flip scattering exists, the conductance spectrum is enhanced to a maximum value. The spin polarization of current in the metallic regime is increased with the strength of the spin-flip scattering to a maximum value. In the tunneling regime, the 1D spin polarization of current is weakly dependent on the strength of the spin-flip scattering. On the contrary, the 2D and 3D spin polarization of current is increased with the strength of the spin-flip scattering until it reaches a higher maximum value than in the metallic limit. In two-band model, s-band and d-band coupling is considered. The spin-flip scattering is ignored. If the coupling is zero, the two bands can cross at some points in the energy spectra. When the coupling between bands is non-zero, a gap is opened up at the crossing points. There are kinks appearing in the density of states corresponding to the crossing points. In both regimes, the conductance is largest, when the effective mass of electron in the majority band of the ferromagnet material is about the same as that of metal.

School of Physics

Academic Year 2010

Student's Signature \_\_\_\_\_

Advisor's Signature \_\_\_\_\_

## ACKNOWLEDGEMENTS

Firstly, I would like to thank my parents, my older brother, and my girlfriend. Their support and encouragement are greatly appreciated.

I have been doing my research on the theoretical study of the tunneling spectroscopy in material such as metals, superconductors, and ferromagnets under Assoc. Prof. Dr. P. Pairor's supervision. I am thankful to my supervisor for her guidance throughout my research years at SUT. Also, I would like to thank Dr. Michael Smith, for his useful comments on our work.

In 2009, I went to the University of Toronto (U of T) in Canada to do an interesting research on superconducting materials under Prof. John Wei's supervision. At U of T, I saw a fantastic superconductivity laboratory but this was not suitable for my work. So, Prof. Wei sent me to Prof. Bill Atkinson who work at Trent University. I am grateful to both Prof. John Wei and Prof. Bill Atkinson for their guidance, patience, and kindness. Also, I would like to thank Dr. Joe Ngai, Prof. Wei's postdoc, for sharing his the beautiful experimental data of the tunneling spectroscopy of high temperature superconductor of  $Y_{1-y}Ca_yBa_2Cu_3O_{7-\delta}$  (YBCO with Ca – doping).

Finally, I would like to acknowledge the financial support from the Commission on Higher Education Grant, Thailand (Grant No. 12/2548), the Research, Development and Engineering (RD&E) Fund through National Nanotechnology Center (NANOTEC), National Science and Technology Development Agency (NSTDA), Thailand (Project No. NN-B-22-DI1-20-51-05) to SUT.

Krisakron Pasanai

# CONTENTS

	<b>Page</b>
ABSTRACT IN THAI . . . . .	I
ABSTRACT IN ENGLISH . . . . .	III
ACKNOWLEDGEMENTS . . . . .	IV
CONTENTS . . . . .	IV
LIST OF TABLES . . . . .	VI
LIST OF FIGURES . . . . .	VII
LIST OF SYMBOLS . . . . .	XII
<b>CHAPTER</b>	
<b>I INTRODUCTION . . . . .</b>	<b>1</b>
1.1 Motivation . . . . .	1
1.2 Outline of thesis . . . . .	8
<b>II CHARGE AND SPIN TRANSPORT OF M/FM JUNCTION     WITHIN A ONE-BAND MODEL . . . . .</b>	<b>9</b>
2.1 Introduction . . . . .	9
2.2 Model and formulation . . . . .	11
2.2.1 The wave functions . . . . .	11
2.2.2 Reflection and transmission probabilities . . . . .	15
2.2.3 Current density and conductance . . . . .	16
2.3 Results and discussion . . . . .	18
2.3.1 Total conductance . . . . .	19
2.3.2 Spin polarization of conductance and current . . . . .	25
2.4 Conclusions . . . . .	31

## CONTENTS (Continued)

	Page
<b>III ELECTRONIC PROPERTIES OF FERROMAGNET WITHIN</b>	
<b>A TWO-BAND MODEL . . . . .</b>	32
3.1 s-d band coupling Hamiltonian . . . . .	32
3.2 Energy dispersion relation . . . . .	36
3.3 Density of states . . . . .	39
3.3.1 DOS in the one-band model . . . . .	39
3.3.2 DOS in the two-band model . . . . .	41
3.4 Conclusions . . . . .	46
<b>IV TUNNELING SPECTROSCOPY IN THE TWO-BAND AP-</b>	
<b>PROXIMATION . . . . .</b>	47
4.1 The wave functions . . . . .	47
4.1.1 The matching conditions . . . . .	52
4.1.2 Reflection and transmission probabilities . . . . .	53
4.2 Results and discussion . . . . .	54
4.3 Conclusions . . . . .	58
<b>V CONCLUSIONS . . . . .</b>	59
REFERENCES . . . . .	62
CURRICULUM VITAE . . . . .	70

## LIST OF TABLES

Table		Page
1.1	Valence electron distribution in 3d and 4s shells in some transition elements. . . . .	7
1.2	Saturation magnetization in 3d metals, where n is the number of electron per atom of 3d and 4s, the magnetic moments per atom is expressed by $\mu_H$ . The data are taken from Introduction to Magnetic Materials (Cullity and Graham, 2008). . . . .	7
3.1	The exchange energies of some ferromagnetic materials. $E_{ex}^s$ is the exchange energy in s-band, while $E_{ex}^d$ is that in d-band. The data are taken from D. Y. Petrovykh et al. (Petrovykh et al., 1998) and J. Callaway and C. S. Wang (Callaway and Wang, 1977). . . . .	34
3.2	The electron $m_e^*$ and hole $m_h^*$ effective masses in direct band gap semiconductors and some ferromagnets. The data are taken from Introduction to solid state physics (Kittel, 2005). . . . .	38
3.3	Carrier mobilities at room temperature of some materials, in $cm^2/V - s$ . The data is taken from Introduction to solid state physics (Kittel, 2005). . . . .	38

# LIST OF FIGURES

Figure	Page	
1.1	As the interatomic distance $d$ is decreased to $d_0$ , the 4s and 3d levels form energy bands. Taken from Solid State Physics (Ashcroft and Mermin, 2003). . . . .	4
1.2	Schematic description of the density of states of 3d (wide) and 4s (narrow) bands. Taken from Solid State Physics (Ashcroft and Mermin, 2003). . . . .	5
1.3	Band structure of Fe. Solid lines refer to energy dispersion of spin-up (majority spin band) while dash lines refer to spin-down band (minority spin band). The data are taken from J. Callaway and C. S. Wang (Callaway and Wang, 1977). The exchange energy $E_{ex}$ in each band can be fitted from this figure. The s band is indicated by number 1, while number 2 or 3 refers to the d band. The hybridization between s-band and d-band occurs around the energy around -0.7 - -0.8 Rydberg. . . . .	5
1.4	Band structure of ferromagnetic Ni. Solid lines refer to energy dispersion of spin-up (majority spin band) while dash lines refer to spin-down band (minority spin band). The hybridization region occur around Fermi level. The data are taken from J. Callaway and C. S. Wang (Wang and Callaway, 1977). . . . .	6
1.5	Brillouin zone of (a) fcc ferromagnetic and (b) bcc ferromagnetic Fe. Taken from Solid State Physics (Ashcroft and Mermin, 2003). . . . .	6

## LIST OF FIGURES (Continued)

Figure		Page
2.1	<p>The sketches of (a) the geometries of 1D, 2D, and 3D M/FM junctions, and (b) the energy spectra of electrons in a metal (left) and in a ferromagnetic material (right). <math>E_F</math>, <math>E_{ex}</math>, and <math>E_0</math> are the Fermi energy of the metal, the ferromagnetic exchange energy and the off-set energy, respectively. The zero is set to be the Fermi level of the metal. The circles, with arrows pointing left or right, represent same-energy quasi-particle states that are considered in the scattering process. <math>a</math> and <math>b</math> denote the incident and reflected states, spin orientation of which can be either up or down. <math>c</math> and <math>d</math> are the spin down and spin up outgoing states, respectively. . . . .</p>	11
2.2	<p>Plots of total conductance spectra <math>G_{total}</math> (solid curves) and their corresponding derivatives <math>E_{ex}[dG_{total}/d(eV)]</math> (dashed curves) in (a) 1D, (b) 2D, and (c) 3D system. <math>Z_0</math> and <math>Z_f</math> are set to be zero. . . . .</p>	20
2.3	<p>Plots of 1D total conductance spectra <math>G_{total}^{1D}</math> as a function of applied potential energy <math>eV</math>. <math>0 \leq Z_f \leq 2</math>. In (a), <math>Z_0 = 0.0</math>, in (b), <math>Z_0 = 0.5</math>, and in (c), <math>Z_0 = 1.0</math>. . . . .</p>	21
2.4	<p>Plots of 2D total conductance spectra <math>G_{total}^{1D}</math> as a function of applied potential energy <math>eV</math>. <math>0 \leq Z_f \leq 2</math> for three different values of the parameter <math>Z_0</math>. In (a), <math>Z_0 = 0.0</math>, in (b), <math>Z_0 = 0.5</math>, and in (c), <math>Z_0 = 1.0</math>. . . . .</p>	22
2.5	<p>Plots of 3D total conductance spectra <math>G_{total}^{1D}</math> as a function of applied potential energy <math>eV</math>. <math>0 \leq Z_f \leq 2</math> for three different values of the parameter <math>Z_0</math>. In (a), <math>Z_0 = 0.0</math>, in (b), <math>Z_0 = 0.5</math>, and in (c), <math>Z_0 = 1.0</math>. . . . .</p>	23

## LIST OF FIGURES (Continued)

Figure		Page
2.6	Plots of 1D total conductance spectra $G_{total}^{1D}$ at $eV = 3E_{ex}$ as a function of spin-flip scattering strength parameter $Z_f$ for various values of spin-flip scattering strength parameter $Z_0$ . . . . .	24
2.7	Plots of spin polarization of conductance spectra as a function of applied potential energy $eV$ in (a) 1D, (b) 2D, and (c) 3D system for $Z_0 = 0$ and $0 \leq Z_f \leq 2$ . . . . .	26
2.8	Plots of spin polarization of current as a function of applied potential energy $eV$ in (a) 1D, (b) 2D, and (c) 3D system for $Z_0 = 0$ and $0 \leq Z_f \leq 2$ . . . . .	27
2.9	Plots of spin polarization of current $P_I^{nD}$ as a function of potential strength $Z_0$ in (a) 1D, (b) 2D, and (c) 3D system for various the spin-flip scattering $0 \leq Z_f \leq 5$ . . . . .	28
2.10	Plots of 1D spin polarization of current $P_I^{nD}$ as a function of (a) potential strength $Z_0$ and $0 \leq Z_f \leq 5$ and (b) spin-flip scattering $Z_f$ and $0 \leq Z_0 \leq 5$ . . . . .	29
3.1	Energy dispersion relations of ferromagnet in a two-band model. In these plots, we take $E_{ex}^d = 0.2 eV$ , $E_{ex}^s = 0.1 eV$ , $E_0^s = 0.1 eV$ , $E_0^d = 0.5 eV$ , and the electron effective masses in d-band and s-band are $m_d^* = 0.5m_e$ and $m_s^* = 0.3m_e$ , respectively, where $m_e$ is electron mass. The coupling between the same spin bands are taken to be (a) $t = 0 eV$ , and (b) $t = 0.05 eV$ . In (a), the crossing points occur at different energy bands as indicated by arrows. In (b), the corresponding avoiding crossing points are indicated by solid arrows. . . . .	37

## LIST OF FIGURES (Continued)

Figure		Page
3.2	Energy dispersion relations of two-band ferromagnet. The exchange energies and the effective mass of s and d-band are the same as in Figure 3.1. In (a) $t = 0.1 \text{ eV}$ and (b) $t = 0.2 \text{ eV}$ . . . . .	40
3.3	Density of states in one-band model. $E_{ex} = 0.2 \text{ eV}$ , $\rho_0$ are $\sqrt{m^*/8\pi^2\hbar^2}$ , $m^*/4\pi\hbar^2$ , and $\sqrt{2m^{*3}/4\pi^4\hbar^6}$ for 1D, 2D, and 3D system respectively. . . . .	41
3.4	The DOS of two-band ferromagnet when $t = 0$ are plotted for (a) 1D, (b) 2D, and (c) 3D system. Parameters are for $E_{ex}^d = 0.2 \text{ eV}$ , $E_{ex}^s = 0.1 \text{ eV}$ , $E_0^s = 0.1 \text{ eV}$ , $E_0^d = 0.5 \text{ eV}$ , $m_d^* = 0.5m_e$ and $m_s^* = 0.3m_e$ , respectively, where $m_e$ is electron mass. . . . .	42
3.5	The DOS of two-band system are plotted for (a) 1D, (b) 2D, and (c) 3D systems. The exchange energies and the electron effective masses are the same as in Figure 3.4, but $t = 0.05 \text{ eV}$ . Subscript <i>mix</i> refers to s-d mixing system. . . . .	43
3.6	The DOS of two-bands ferromagnet are plotted for (a) 1D, (b) 2D, and (c) 3D systems. The exchange energies and the electron effective masses are the same as in Figure 3.4, but $t = 0.1 \text{ eV}$ . . . . .	44
3.7	The the DOS of two-bands ferromagnet are plotted for (a) 1D, (b) 2D, and (c) 3D systems. The exchange energies and the electron effective masses are the same as in Figure 3.4, but $t = 0.2 \text{ eV}$ . . . . .	45
4.1	Schematic illustration of the energy dispersion relation of one-band metal/two-band ferromagnet junction. The potential at the interface is defined by a delta potential $U\delta(x)$ . $E_F = 10E_{ex}^d$ , $t = 0.05 \text{ eV}$ . . . . .	49

## LIST OF FIGURES (Continued)

Figure		Page
4.2	The sketch of probabilities across the M/FM junction, where ( $l$ ) refers to the four injection processes, and $i$ refers to reflected as electron with spin-up ( $i = 1, 3$ ) and spin-down ( $i = 2, 4$ ). . . . .	54
4.3	Plot of the conductance spectra $G$ as a function of energy $E$ . Parameters are for $Z_0 = 0$ , $E_{ex}^s = 0.1$ eV, $E_{ex}^d = 0.2$ eV, $E_0^s = 0.1$ eV, $E_0^d = 0.5$ eV, $m_M^* = 0.5m_e$ , $m_d^* = 0.5m_e$ , $m_s^* = 0.3m_e$ . The coupling strength $t$ is zero. Solid arrows are indicated the bottom of each corresponding band. . . . .	55
4.4	Plots of the conductance spectra $G$ as a function of energy $E$ . Parameters are for $Z_0 = 0$ , $E_0^s = 0.1$ , $E_0^d = 0.5$ , $E_{ex}^s = 0.1$ , $E_{ex}^d = 0.2$ , $m_M^* = 0.5m_e$ , $m_d^* = 0.5m_e$ , $m_s^* = 0.3m_e$ . In (a) $t = 0.05$ eV, (b) $t = 0.1$ eV, and (c) $t = 0.2$ eV. Solid arrows are indicated the bottom of each corresponding band. . . . .	56
4.5	Plots of the conductance spectra $G$ as a function of applied biased voltage $eV$ for various $Z_0$ . The exchange energies and the electron effective masses are the same as in Figure 4.4, but $t = 0.05$ eV. . . . .	57
4.6	Plot of the conductance spectra $G$ as a function of biased voltage $eV$ for various of the effective masses in metal $m_M^*$ . Parameters are for $Z_0 = 0.0$ , $E_0^s = 0.1$ eV, $E_0^d = 0.5$ eV, $E_{ex}^s = 0.1$ eV, $E_{ex}^d = 0.2$ eV. The electron effective masses in ferromagnet are $m_d^* = 0.5m_e$ , $m_s^* = 0.3m_e$ fixed, where $m_e$ is electron mass. . . . .	58

## LIST OF SYMBOLS

$k$	Momentum amplitude
$\hbar$	Plank constant
$j$	Current density
$G$	Conductance
$eV$	Bias voltage
$P$	Polarization
$Z$	Potential strength at the interface
$Z_f$	Spin-flip scattering at the interface
$\xi_k$	Kinetic energy
$t_{(\sigma\sigma),(\sigma\hat{\sigma})}$	Coupling strength between energy bands
$\lambda$	Eigenvalues of s-d mixing band
$\psi_\sigma$	Quantum-mechanical wave function with spin $\sigma$
$m^*$	Electron effective mass in material
$E_0$	Off-set energy
$E_F$	Fermi energy
$E_{ex}$	Exchange energy
$\mu$	Electron mobility
$\rho$	Density of state
$\Theta$	Heaviside step function

# CHAPTER I

## INTRODUCTION

### 1.1 Motivation

In the past three decades, an exciting field called *spintronics* has emerged. It involves the study of using electron spin, in addition to charge, to control the motion of electron (Prinz, 1959; Žutić et al., 2004; Fert, 2008). Among many applications of spintronics devices are the read heads of hard disks greatly contributed to the fast rise in the density of stored information and led to the extension of the hard disk technology to consumer's electronics. These devices are constructed from layers of alternating ferromagnetic and non-magnetic materials, which exhibit giant magnetoresistance (GMR)(Binasch et al., 1989; Baibich et al., 1988). That is, the resistance of the layers strongly depends on the magnetization direction in the magnetic layers. The resistance is much larger when the magnetizations of the two adjacent magnetic layers are opposite in direction than when they are in the same direction.

Since the discovery of GMR, the electron charge and spin transport properties across the interface between metal and ferromagnetic material have been extensively studied. Theoretical calculations of this type of junction have assumed one-band dispersion model for ferromagnet. For instance, in the study of Andreev reflection at a ferromagnet/superconductor interface (Kashiwaya et al., 1999; de Jong and Beenakker, 1995), it was found that the Andreev reflection can occur at the interface and is strongly affected by the exchange energy of the ferromagnet. The double junction systems of ferromagnet/superconductor/ferromagnet are also studied by many groups (Yamashita et al., 2003; Dong et al., 2003; Dong et al., 2002; Božović and Radović, 2002). They studied the effect of different parameters on charge and

spin transport of this system. It was mainly found that if the thickness of the superconducting layer is less than the coherence length of the superconductor, then the spin polarization is unaffected by the superconducting layer (Yamashita et al., 2003). Thus, to obtain a high spin polarization of conductance, one needs to make the superconducting layer thinner than its coherence length. In the study of ferromagnet/metal/superconductor double junctions by Ohtori and Imamura (Ohtori and Imamura, 2009), it was found that the exchange energy and the spin polarization of a ferromagnet can be determined from the period of the conductance oscillation.

The conductance spectra in ferromagnet and other materials like two-dimensional electron gas with Rashba spin-orbit coupling were also studied within one-band approximation model (Larsen et al., 2002; Matsuyama et al., 2002). It was found that the conductance spectra can be modulated by either changing the magnetization directions or the Rashba coupling strength. In all of the above studies, it was assumed that the itinerant electrons come from the d band and those from the s band are completely neglected because the density of states of d-band electrons is much larger than that of the s-band electrons (Matsuyama et al., 2002; Petrovykh et al., 1998; Stoner, 1938; Stoner, 1933). Therefore, the conductivity and magnetism properties are mainly as a result of these electrons. In addition, the exchange energy, the splitting between the energies of the majority-spin electrons and minority-spin electrons, in the d-band  $E_{ex}^d$  is much larger than that in the s-band  $E_{ex}^s$  as illustrated, in Figures 1.3 - 1.4 (Nautiyal and Auluck, 1986; Nautiyal and Auluck, 1985; Turner et al., 1984; Callaway and Wang, 1977; Wang and Callaway, 1977; Pessa et al., 1975; Batallan et al., 1975; Wang and Callaway, 1974; Mijnders, 1973; Zornberg, 1970). However, the existence of the s-band electrons can affect the transport properties in some cases and it is worth considering.

The band structure calculations of two ferromagnets Fe and Ni are shown in Figures 1.3 - 1.4. As can be seen in both figures, there are coupling regions between

the s-band and d-band energy dispersions near the Fermi level, called s-d mixing. In these figures, the band structures are shown along the most important lines of symmetry in the Brillouin zone. We can distinguish parabola, starting from  $\Gamma$  and continuing above  $E_F$ . Consequently, they represent the band of the 4s electrons, which overlaps the band of 3d electrons and the Fermi energy lies in both bands. So that, s-d mixing is inevitable.

There are other ferromagnets found in the recent experiments. For instance,  $\text{Ga}_{1-x}\text{Mn}_x\text{As}$  exhibits hysteretic electroluminescence polarization (Ohno et al., 1999). Technically, in this ferromagnetic semiconductor the Fermi level and the exchange energy can be changed by changing doping concentration (Petrovykh et al., 2007). This means the electrons from the s band can also conduct electricity in this material and both s-band and d-band electrons can affect the electronic properties.

The main focus of this work is to take into account both s and d-band electrons by developing an alternative way, a two-band approximation, to study transport properties of a metal/ferromagnetic material junction. In particular, we will give the answers to the following main questions.

- When do we need a two-band model in describing a ferromagnetic material?
- What are the new features detectable in charge transport when a two-band model is included?

Two-band model has been used in other materials like  $\text{Y}_{1-y}\text{Ca}_y\text{Ba}_2\text{Cu}_3\text{O}_{1-\delta}$  (YBCO with Ca-doping) (Pasanai and Atkinson, 2010; Ngai et al., 2007). K. Pasanai and W. A. Atkinson showed that chain (one-dimensional system of CuO) can become superconductivity due to the proximity (coupling) effect between chain and plane (two-dimensional system of  $\text{CuO}_2$ ) layers. Consequently, the effect of the coupling strength between chain and plane layers makes the energy dispersion of a chain and a plane layer change. This change strongly depends on how big of the coupling strength between bands. This idea is very similar to what happen in ferromagnetic materials.

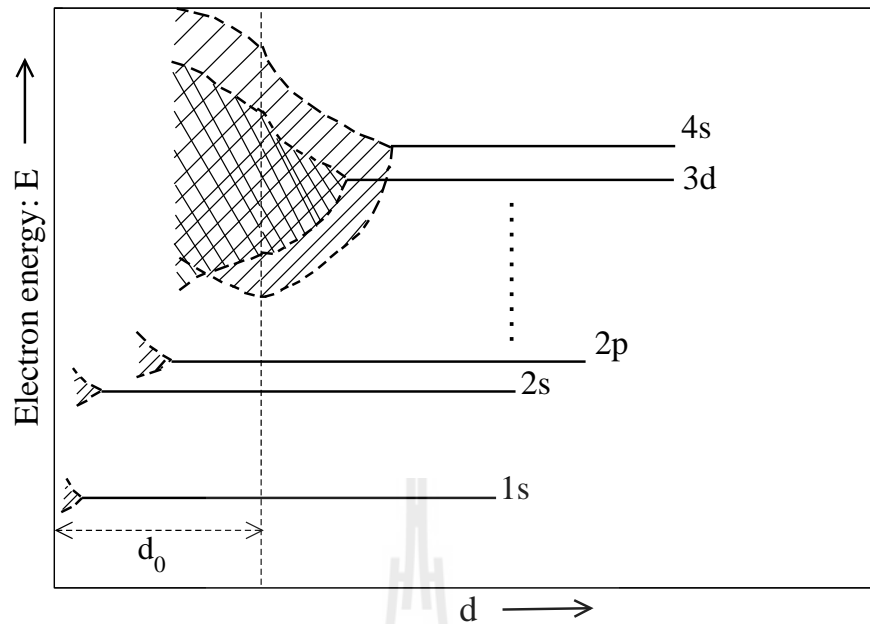


**Figure 1.1** As the interatomic distance  $d$  is decreased to  $d_0$ , the 4s and 3d levels form energy bands. Taken from Solid State Physics (Ashcroft and Mermin, 2003).

The physics of a coupling between energy bands in a solid can be understood as follows. When two atoms are brought close together to form a solid, the positions of the energy levels are modified. When two atoms are well separated, their, for example, 1s shells (each containing two electrons) have exactly the same energy. When they are closer, their electron clouds begin to overlap and the 1s shells are now split into two levels with two electrons in each. When  $N$  atoms come together, these shells from  $N$  atoms will form bands,  $N$  levels packed closely each other. The extent of the splitting between each level is different for a different shells as indicated in Figure 1.1. In transition elements, the outermost electrons in the transition elements are in 3d and 4s shells, and when they are brought together until the interatomic distance is  $d_0$ , they are the first to overlap and the corresponding levels form a band as shown in the figure. The 3d band is narrower than the 4s band because the 4s electrons are farther from the nucleus. Technically, experimental evidence for above statements was found by the X-ray emission spectra of solid metal (Piper et al., 2010; Kobayashi et al., 2008; Okabayashi et al., 2001; Fujioka et al., 1997).

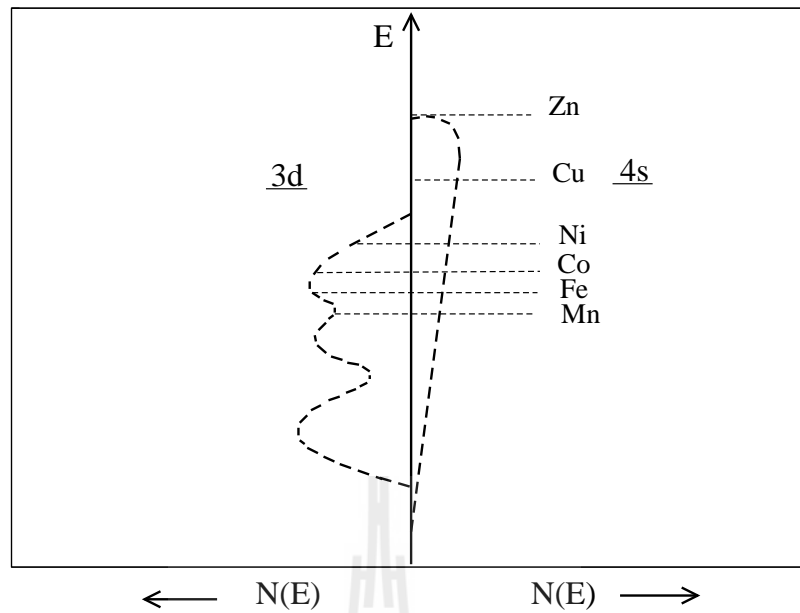


**Figure 1.2** Schematic description of the density of states of 3d (wide) and 4s (narrow) bands. Taken from Solid State Physics (Ashcroft and Mermin, 2003).

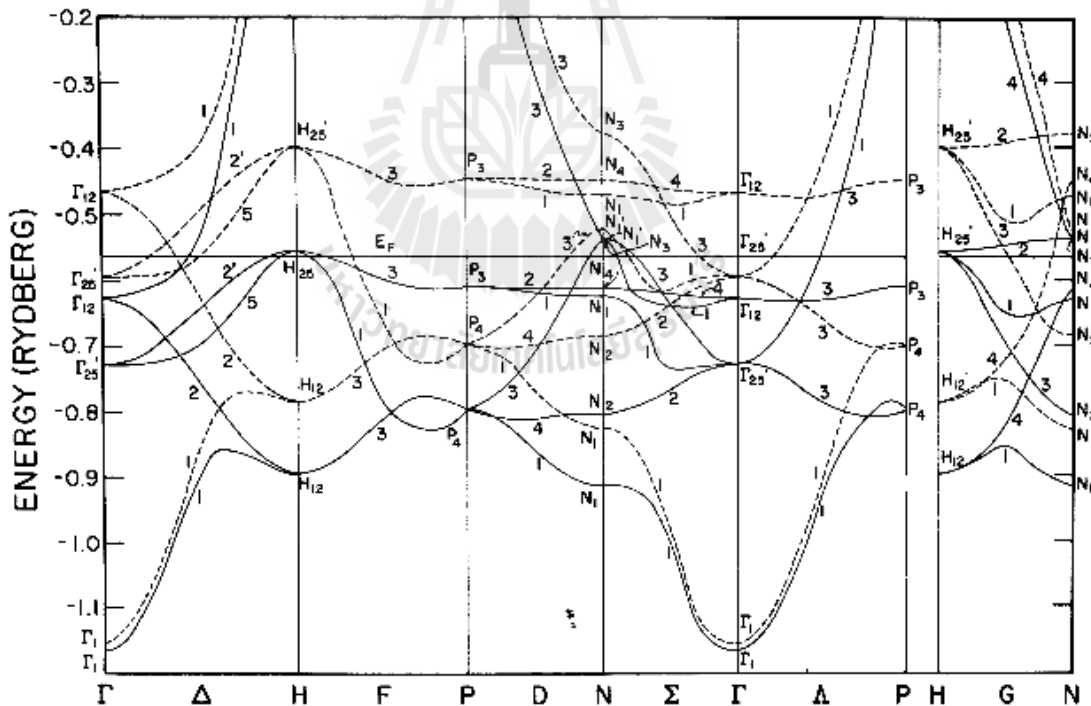


**Figure 1.3** Band structure of Fe. Solid lines refer to energy dispersion of spin-up (majority spin band) while dash lines refer to spin-down band (minority spin band). The data are taken from J. Callaway and C. S. Wang (Callaway and Wang, 1977). The exchange energy  $E_{ex}$  in each band can be fitted from this figure. The s band is indicated by number 1, while number 2 or 3 refers to the d band. The hybridization between s-band and d-band occurs around the energy around -0.7 - -0.8 Rydberg.



**Table 1.1** Valence electron distribution in 3d and 4s shells in some transition elements.

Number of electrons in Shell	Ti	V	Cr	Mn	Fe	Co	Ni
3d	2	3	5	5	6	7	8
4s	2	2	1	2	2	2	2

**Table 1.2** Saturation magnetization in 3d metals, where n is the number of electron per atom of 3d and 4s, the magnetic moments per atom is expressed by  $\mu_H$ . The data are taken from Introduction to Magnetic Materials (Cullity and Graham, 2008).

	Mn	Fe	Co	Ni	Cu
n	7	8	9	10	11
$\mu_H$ (observed) ( $\mu_B/atom$ )	0	2.22	1.72	0.60	0
$\mu_H$ (calculated) ( $\mu_B/atom$ )	3.60	2.60	1.60	0.60	-0.40

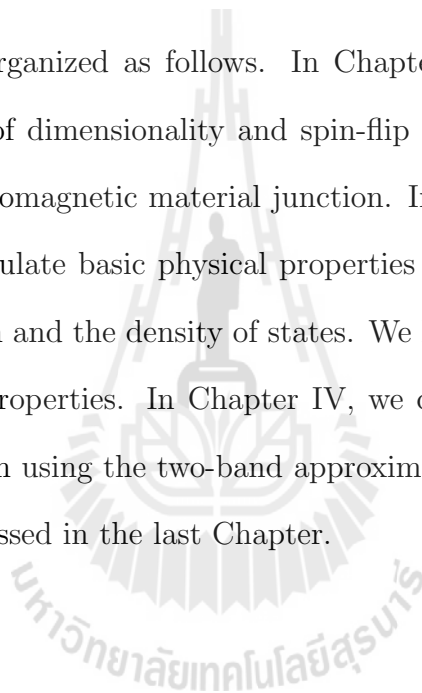
In Figures 1.3 - 1.4, the band structures of Fe and Ni are shown respectively. It can be seen that the exchange energy of Fe is larger than that of Ni. The dispersion relations in Figures 1.3 - 1.4 also show that the exchange energy (the energy between spin-up and spin-down) at the bottom of the d band are larger than that in the s band, but they are almost the same value at the hybridization region (the mixing between s-band and d-band region).

A short conclusion here is that the tunneling spectroscopy calculations in the past were only considered the electrons that live near the Fermi level and carry a large magnetization. Because of this reason, the electrons from the s band are completely neglected in those calculations. Interestingly, if the Fermi level and exchange splitting in the s band  $E_{ex}^s$  can be changed in a ferromagnet semiconductor, by changing doping concentration, then the electron from this band has to be taken into account in the calculation. In this thesis, the tunneling spectroscopy of ferromagnetic materials will be studied using a two-band (s-d mixing) model.

## 1.2 Outline of thesis

The main focus of this thesis is to use an alternative model to study of the tunneling spectroscopy of ferromagnetic materials. The main calculations concern with the density of states and the conductance spectra of a hybridization between s-band and d-band dispersion relations (s-d mixing) within the free electron approximation model. The main results of these calculations will be compared with those from one-band model.

This thesis is organized as follows. In Chapter II, we use one-band model to consider the effect of dimensionality and spin-flip scattering on charge and spin transport of metal/ferromagnetic material junction. In Chapter III, we consider s-d mixing model and calculate basic physical properties of a ferromagnet like, the energy dispersion relation and the density of states. We look into how the s-d coupling strength affect these properties. In Chapter IV, we calculated the tunneling spectroscopy of the junction using the two-band approximation. Finally, the conclusions of this thesis are addressed in the last Chapter.



# CHAPTER II

## CHARGE AND SPIN TRANSPORT OF M/FM JUNCTION WITHIN A ONE-BAND MODEL

### 2.1 Introduction

Since the discovery of giant magnetoresistance, the electron charge and spin transport properties across metal/ferromagnetic material (M/FM) interface have been extensively studied (Fert, 2008; Grunberg, 2008). It is known that the moving magnetization of a ferromagnet pumps a spin current into the attached metal (Tserkovnyak et al., 2002). Nonetheless, conversion of excess spins occurs even when the interface is transparent and results in a spin accumulation that decays over the spin-flip diffusion lengths in both materials (van Son et al., 1987). This effect causes the spin-coupled interface resistance (Jedema et al., 2003), and makes the spin diffusion length in the ferromagnetic material the limiting factor to obtain a large spin polarization. This problem, called the conductivity mismatch, leads to the poor efficiency of spin injection from a metallic ferromagnet into a semiconductor (Schmidt et al., 2000; Filip et al., 2000). Surprisingly, a way to enhance the efficiency is to insert a thin insulating layer between the two materials (Filip et al., 2000; Fert and Jaffrès, 2001; Rashba, 2000). The inserted layer acts as a tunnel barrier for the electrons to scatter without spin flipping. These studies suggest that the interface properties play a crucial role in determining the efficiency of both charge and spin transport.

In addition to the non-spin-flip scattering, electrons can undergo a spin-flip scattering at the interface as well. This type of scattering can be created by embed-

ding magnetic impurities at the interface (Guinea, 1998; Lyu et al., 1998; Jansen and Moodera, 2000; Vedyayev et al., 2001). In the presence of spin-flip scattering, spin-up and spin-down states are coupled and there are some consequences of this coupling. For instance, the non-spin-flip scattering, when present alone, is found to suppress the conductance of a metal/two-dimensional electron gas junction. However, when the spin-flip scattering is also present, the conductance can be increased with the strength of the non-spin-flip scattering (Srisongmuang et al., 2008). Similarly, in the study of the tunneling magnetoresistance of a nonmagnetic metal island sandwiched by two ferromagnetic electrodes, asymmetry between the interface spin-flip strengths of spin-up and spin-down electrons can result in an enhancement in the tunnel magnetoresistance (Ma et al., 2009; Ma et al., 2010). In a FM/SC junction, the absence of current perpendicular to the plane magnetoresistance was predicted due to Andreev reflection at the interface in phase coherent theory (Taddei et al., 1999). This prediction was in contradiction with what was observed in magnetic multilayers sandwiched between superconducting electrodes (Pratt et al., 1991). By an inclusion of a small amount of interfacial spin-flip scattering, the giant magnetoresistance effect with a superconductor contact can be explained (Wang et al., 2010).

In this chapter, using a scattering theory, we study the impact of the interfacial spin-flip scattering on charge and spin transport across M/FM interface in one, two and three-dimensional systems. Specifically, we calculate their total conductance and the spin polarization of conductance spectra and current. As in previous work on a metal/Rashba system junction (Srisongmuang et al., 2008), in some circumstances we find the spin-flip scattering can help increase both the total conductance and spin-polarization of conductance. Whereas the behavior of the enhancement of the total conductance are similar in all dimensional cases, for the spin polarization of conductance the behavior of its enhancement in one-dimensional (1D) system is very different from that in two-dimensional (2D) and three-dimensional (3D) systems.

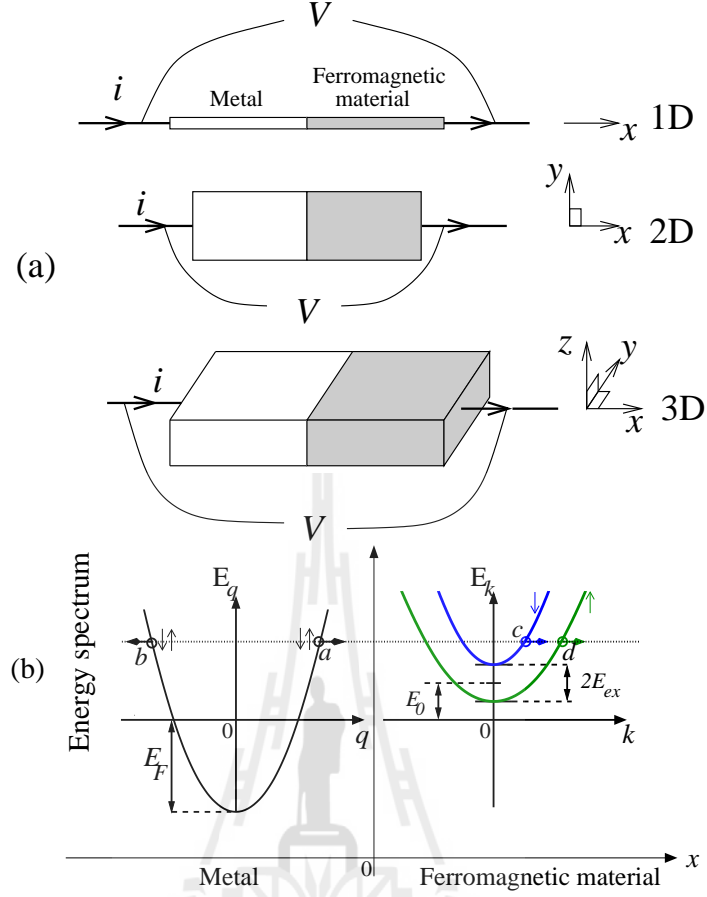


**Figure 2.1** The sketches of (a) the geometries of 1D, 2D, and 3D M/FM junctions, and (b) the energy spectra of electrons in a metal (left) and in a ferromagnetic material (right).  $E_F$ ,  $E_{ex}$ , and  $E_0$  are the Fermi energy of the metal, the ferromagnetic exchange energy and the off-set energy, respectively. The zero is set to be the Fermi level of the metal. The circles, with arrows pointing left or right, represent same-energy quasiparticle states that are considered in the scattering process.  $a$  and  $b$  denote the incident and reflected states, spin orientation of which can be either up or down.  $c$  and  $d$  are the spin down and spin up outgoing states, respectively.

## 2.2 Model and formulation

### 2.2.1 The wave functions

In this work, M/FM junction system is illustrated in Figure 2.1. In this figure, a normal metal is in  $x < 0$  region while a ferromagnet is in  $x > 0$  region, each of which can be represented by an infinite 1D, 2D, and 3D dimensional systems. The current in the system flows along the  $x$  direction. For simplicity, the potential at the interface is modeled by the Dirac delta function. The spin-flip scattering at the

interface is also considered in this study. In the calculation, we consider the ballistic regime and only use the one-band approximation.

The Hamiltonian of the system is given by the following expression.

$$H(x) = \left( \frac{-\hbar^2}{2} \vec{\nabla} \frac{1}{m(x)} \vec{\nabla} + V(x, y, z) \right) \begin{pmatrix} 1 & 0 \\ 0 & 1 \end{pmatrix} + E_{ex} \hat{m} \cdot \hat{\sigma} \quad (2.1)$$

where  $\vec{\nabla} = \hat{x} \frac{\partial}{\partial x}$  is for 1D system,  $\vec{\nabla} = \hat{x} \frac{\partial}{\partial x} + \hat{y} \frac{\partial}{\partial y}$  is for 2D system, and  $\vec{\nabla} = \hat{x} \frac{\partial}{\partial x} + \hat{y} \frac{\partial}{\partial y} + \hat{z} \frac{\partial}{\partial z}$  is for 3D system. The effective mass  $m(x)$  is position dependent:

$$[m(x)]^{-1} = m^{-1} \Theta(-x) + (m^*)^{-1} \Theta(x), \quad (2.2)$$

where  $m$  and  $m^*$  are electron effective masses in the metal and the ferromagnet, respectively, and  $\Theta(x)$  is the Heaviside step function. The potential barrier is modeled by

$$V(x, y, z) = U \delta(x) + E_0 \Theta(x) - E_F \Theta(-x), \quad (2.3)$$

where  $U = \begin{bmatrix} u_{\uparrow\uparrow} & u_{\uparrow\downarrow} \\ u_{\downarrow\uparrow} & u_{\downarrow\downarrow} \end{bmatrix}$  refers to the scattering potential at the interface,  $\delta(x)$  is the Dirac delta function,  $E_0$  is the off-set energy of ferromagnetic system, and  $E_F$  is Fermi energy in the metal side (see Figure 2.1 for illustration). The exchange energy in the ferromagnet is represented by  $E_{ex}$ . The value of  $E_0$  dictates the energy-state occupancy of electrons in the ferromagnet. That is, when  $E_0 \geq E_{ex}$ , all the energy states are unoccupied, but when  $E_0 \leq E_{ex}$  they are partially occupied. When we consider the conductance spectrum due to applied electric potential energy, the value of  $E_0$  will shift the conductance feature along the applied potential energy axis. In order to see all features coming from the ferromagnetic energy bands, we henceforth set  $E_0 = E_{ex}$ . The vector  $\hat{m}$  denotes the unity vector of the magnetization in the ferromagnetic electrode. In this work, the spin-quantization axis is chosen in the  $\hat{z}$

direction and all spin states are expressed in the basis  $\begin{bmatrix} 1 \\ 0 \end{bmatrix}$ ,  $\begin{bmatrix} 0 \\ 1 \end{bmatrix}$  of the eigenstates with respect to the Pauli matrices  $\sigma_z$ .

For the injection of a given spin degree of freedom from a metal side, the wave function in each region can be written as the linear combination of the injected, and either the reflected or the transmitted eigenstates. Electrons with spin-up and spin-down are equally likely to be injected from the metal side. The wave functions in metal have the following forms.

$$\Psi_M^{(1)}(\vec{r}) = \left( \begin{bmatrix} 1 \\ 0 \end{bmatrix} e^{iq_x x} + \begin{bmatrix} r_{q\uparrow}^{(1)} \\ r_{q\downarrow}^{(1)} \end{bmatrix} e^{-iq_x x} \right) e^{i\vec{q}_{\parallel} \cdot \vec{r}_{\parallel}} \quad (2.4)$$

$$\Psi_M^{(2)}(\vec{r}) = \left( \begin{bmatrix} 0 \\ 1 \end{bmatrix} e^{iq_x x} + \begin{bmatrix} r_{q\uparrow}^{(2)} \\ r_{q\downarrow}^{(2)} \end{bmatrix} e^{-iq_x x} \right) e^{i\vec{q}_{\parallel} \cdot \vec{r}_{\parallel}} \quad (2.5)$$

where  $r_{q\sigma}^{(i)}$  are the amplitudes of reflected states with spin  $\sigma$  for the incident state with spin-up ( $i = 1$ ) and spin-down ( $i = 2$ ) and  $r_{\parallel}$  is a position vector along the line or plane of the interface, depending on the dimensionality of the system. In 1D case,  $q_x = q$  and  $q_{\parallel} = 0$ . In 2D case,  $q_x = q \cos \phi_q$ , and  $q_{\parallel} = q \sin \phi_q$ , where  $\phi_q$  are the angle between the wave vectors  $q$  and the  $+x$  direction. In 3D case,  $q_x = q \sin \theta_q \cos \phi_q$  and  $q_{\parallel} = \hat{z}q \cos \theta_q + \hat{y}q \sin \theta_q \sin \phi_q$ , where  $\theta_q$  is the angle between the wave vector  $q$  and the  $+z$  direction and  $\phi_q$  is the angle between the projection of the wave vector  $q$  on the  $xy$  plane and the  $+x$  direction.

Similarly, due to the ballistic scattering, we obtain the quasiparticle wave function in the ferromagnetic region as a linear combination of two outgoing states with the same energy and the same  $k_{\parallel}$  as those of the incident state:

$$\Psi_{FM}^{(i)}(r) = \left( \begin{bmatrix} t_{k\uparrow}^{(i)} \\ 0 \end{bmatrix} e^{ik_x x} + \begin{bmatrix} 0 \\ t_{k\downarrow}^{(i)} \end{bmatrix} e^{ik_x x} \right) e^{i\vec{k}_{\parallel} \cdot \vec{r}_{\parallel}} \quad (2.6)$$

where  $i = 1, 2$  refer to the wave function of the ferromagnetic material corresponding to the two cases of spin orientations of the incident electrons.  $t_{k\sigma}^{(i)}$  are the transmission amplitudes of electrons to  $\sigma$ -spin state. Like the electron wave vector in metal,  $k_{x\sigma} = k_\sigma$  and  $k_{\parallel} = 0$  in 1D case. In 2D case,  $k_{x\sigma} = k_\sigma \cos \phi_{k\sigma}$ , and because of the translation symmetry along the interface, the momentum parallel to the interface is conserved, i. e.  $k_{\parallel} = k_\sigma \sin \phi_{k\sigma} = q_{\parallel}$ , where  $\phi_{k\sigma}$  are the angles between the wave vectors  $k_\sigma$  and the  $+x$  direction. In 3D case,  $k_{x\sigma} = k_\sigma \sin \theta_{k\sigma} \cos \phi_{k\sigma}$  and  $k_{\parallel} = \hat{z}k_\sigma \cos \theta_{k\sigma} + \hat{y}k_\sigma \sin \theta_{k\sigma} \sin \phi_{k\sigma} = q_{\parallel}$ , where  $\theta_{k\sigma}$  is the angle between the wave vector  $k_\sigma$  and the  $+z$  direction and  $\phi_{k\sigma}$  is the angle between the projection of the wave vector  $k_\sigma$  on the  $xy$  plane and the  $+x$  direction.

The relation between the angles are

$$q \sin[\theta_q] = k_{\uparrow} \sin[\theta_{k_{\uparrow}}] = k_{\downarrow} \sin[\theta_{k_{\downarrow}}] \quad (2.7)$$

for 2D system, and

$$q \cos[\phi_q] = k_{\uparrow} \cos[\phi_{k_{\uparrow}}] = k_{\downarrow} \cos[\phi_{k_{\downarrow}}] \quad (2.8)$$

$$q \sin[\theta_q] \sin[\phi_q] = k_{\uparrow} \sin[\theta_{k_{\uparrow}}] \sin[\phi_{k_{\uparrow}}] = k_{\downarrow} \sin[\theta_{k_{\downarrow}}] \sin[\phi_{k_{\downarrow}}] \quad (2.9)$$

for 3D system.

All coefficients,  $r_{q\sigma}$  and  $t_{k\sigma}$ , can be obtained from the appropriate matching conditions at the interface, which are given by

$$\Psi_M^{(i)}(x = 0, r_{\parallel}) = \Psi_{FM}^{(i)}(x = 0, r_{\parallel}) = \Psi_0^{(i)} \quad (2.10)$$

for the continuity of the wave function at the interface and

$$\left( \frac{m}{m^*} \frac{\partial \Psi_{FM}^{(i)}}{\partial x} - \frac{\partial \Psi_M^{(i)}}{\partial x} \right) \Big|_{x=0} = 2q_F \begin{bmatrix} Z_{\uparrow\uparrow} & Z_{\uparrow\downarrow} \\ Z_{\downarrow\uparrow} & Z_{\downarrow\downarrow} \end{bmatrix} \begin{bmatrix} \Psi_{0\uparrow}^{(i)} \\ \Psi_{0\downarrow}^{(i)} \end{bmatrix} \quad (2.11)$$

for the discontinuity of the slope of the wave function at the interface due to the presence of the Dirac delta potential at the interface. Here the unitless parameter  $Z = mU/\hbar^2 q_F = \begin{bmatrix} Z_{\uparrow\uparrow} & Z_{\uparrow\downarrow} \\ Z_{\downarrow\uparrow} & Z_{\downarrow\downarrow} \end{bmatrix}$ . The potential strength of the spin-up  $Z_{\uparrow\uparrow}$  and spin-down  $Z_{\downarrow\downarrow}$  components are set to be equal ( $Z_{\uparrow\uparrow} = Z_{\downarrow\downarrow} = Z_0$ ). The off-diagonal elements  $Z_{\uparrow\downarrow}$  and  $Z_{\downarrow\uparrow}$  are chosen to be real and equal to ensure the Hermitian property of the Hamiltonian. These off-diagonal elements refer to the spin-flip scattering at the interface  $Z_{\uparrow\downarrow} = Z_{\downarrow\uparrow} \equiv Z_f$ .

## 2.2.2 Reflection and transmission probabilities

The analytical expressions of each coefficient are obtained by using the above matching conditions. That is,

$$t_{k\uparrow} = \frac{2iq}{ik_{\uparrow} - 2q_F Z_0 + iq - \left( \frac{4q_F^2 Z_f^2}{ik_{\downarrow} - 2q_F Z_0 + iq} \right)} \quad (2.12)$$

$$t_{k\downarrow} = \left( \frac{2q_F Z_f}{ik_{\downarrow} - 2q_F Z_0 + iq} \right) t_{\uparrow} \quad (2.13)$$

for the injection of electron with spin-up from the metal side. In this case, the reflection coefficient of the electron with spin-up and spin-down are respectively  $r_{q\uparrow} = t_{k\uparrow} - 1$  and  $r_{q\downarrow} = t_{k\downarrow}$ .

When the incident electron is in spin-down state,

$$t_{k\downarrow} = \frac{2iq}{ik_{\downarrow} - 2q_F Z_0 + iq - \left( \frac{4q_F^2 Z_f^2}{ik_{\uparrow} - 2q_F Z_0 + iq} \right)} \quad (2.14)$$

$$t_{k\uparrow} = \left( \frac{2q_F Z_f}{ik_{\uparrow} - 2q_F Z_0 + iq} \right) t_{k\downarrow} \quad (2.15)$$

Again,  $r_{q\uparrow} = t_{k\uparrow}$  and  $r_{q\downarrow} = t_{k\downarrow} - 1$  in this injection case. Not surprisingly, we can easily interpret that the spin-flip scattering makes the amplitude of the transmission of the opposite spin configuration of the injection spin state non-zero. The reflection and the transmission probabilities of the given spin configuration are

$$R_{q\uparrow(q\downarrow)} = |r_{q\uparrow(q\downarrow)}|^2, \quad (2.16)$$

$$T_{k\uparrow(k\downarrow)} = \left| \frac{k_{\uparrow(\downarrow)}}{q} \right| |t_{k\uparrow(k\downarrow)}|^2. \quad (2.17)$$

### 2.2.3 Current density and conductance

The electric current density is

$$j_{\sigma}^x(eV) = e \sum_{k, k_x > 0} v_{k\sigma}^x T_{k\sigma} [f(E_k - eV) - f(E_k)] \quad (2.18)$$

where  $e$  is the electron charge,  $v_{k\sigma}^x$  is the component of the electron group velocity in the  $x$  direction, and the transmission probability  $T_k = (T_{k\uparrow} + T_{k\downarrow})$ .

In 1D case, Equation 2.18 becomes

$$j_{\sigma}^x(eV) = \frac{eL}{h} \int_0^{\infty} dE_k T_{k\sigma} [f(E_k - eV) - f(E_k)] \quad (2.19)$$

where  $L$  is the size of the ferromagnetic material and  $h$  is Planck's constant. Setting

the temperature to zero, we obtain

$$j_{\sigma}^x(eV) = \frac{eL}{h} \int_0^{eV} dE_k T_{k\sigma}. \quad (2.20)$$

Notice that  $T_{k\sigma}$  is now written as a function of energy  $E_k$ . The corresponding 1D conductance at zero temperature is defined as

$$G_{\sigma}^{1D}(eV) \equiv \frac{1}{L} \frac{dj_{\sigma}^x}{dV} \frac{e^2}{h} T_{k\sigma}(eV) \quad (2.21)$$

In 2D case, the current density at zero temperature is

$$j_{\sigma}^x(eV) = \frac{eL^2}{2\pi h} \int_0^{eV} dE_k \sqrt{\eta[E_k - E_0 + \sigma E_{ex}]} \int_{-\pi}^{\pi} d\varphi_{k\sigma} T_{k\sigma}(E_k, \varphi_{k\sigma}) \cos(\varphi_{k\sigma}) \quad (2.22)$$

where  $\eta = m/m^*$ ,  $L^2$  is the size of the ferromagnetic system, and  $\sigma$  is positive (negative) for spin-up (spin-down) current.  $T_{k\sigma}$  is now a function of energy  $E_k$  and  $\varphi_{k\sigma}$ . The 2D conductance is

$$G_{\sigma}^{2D}(eV) \equiv \frac{2\pi}{q_F L^2} \frac{dj_{\sigma}^x}{dV} = \frac{e^2}{h} \sqrt{\frac{\eta[E_k - E_0 + \sigma E_{ex}]}{E_F}} \int_{-\pi}^{\pi} d\varphi_{k\sigma} T_{k\sigma}(E_k, \varphi_{k\sigma}) \cos(\varphi_{k\sigma}) \quad (2.23)$$

Lastly in 3D case, the current density at zero temperature is

$$\begin{aligned} j_{\sigma}^x(eV) &= \frac{eL^3 q_F^2}{4\pi^2 h} \int_0^{eV} dE_k \sqrt{\frac{\eta[E_k - E_0 + \sigma E_{ex}]}{E_F}} \int_0^{\pi} d\theta_{k\sigma} \sin^2(\theta_{k\sigma}) \\ &\times \int_{-\pi}^{\pi} d\varphi_{k\sigma} T_{k\sigma}(E_k, \theta_{k\sigma}, \varphi_{k\sigma}) \cos(\varphi_{k\sigma}), \end{aligned} \quad (2.24)$$

where  $L^3$  is the size of the ferromagnetic system.  $T_{k\sigma}$  becomes a function of energy

$E_k$ ,  $\theta_{k\sigma}$ , and  $\varphi_{k\sigma}$ . The 3D conductance is

$$G_{\sigma}^{3D}(eV) \equiv \frac{4\pi^2}{q_F^2 L^3} \frac{dj_{\sigma}^x}{dV} = \frac{e^2}{h} \left[ \frac{\eta[E_k - E_0 + \sigma E_{ex}]}{E_F} \right] \int_0^{\pi} d\theta_{k\sigma} \sin^2(\theta_{k\sigma}) \times \int_{-\pi}^{\pi} d\varphi_{k\sigma} T_{k\sigma}(E_k, \theta_{k\sigma}, \varphi_{k\sigma}) \cos(\varphi_{k\sigma}), \quad (2.25)$$

The total conductance in n-dimensional case  $G_{total}^{nD}(eV)$  is the sum of both spin up and spin down conductance, i.e.,  $G_{total}^{nD}(eV) = \sum_{\sigma} G_{\sigma}^{nD}(eV)$

In addition to the total conductance spectrum, the difference between the spin-up and the spin-down conductance and current are considered as well. The spin polarization of conductance  $P_G$  and current  $P_I$  are defined as

$$P_G^{nD}(eV) = \frac{G_{\uparrow}^{nD}(eV) - G_{\downarrow}^{nD}(eV)}{G_{\uparrow}^{nD}(eV) + G_{\downarrow}^{nD}(eV)} \quad (2.26)$$

$$P_I^{nD}(eV) = \frac{j_{\uparrow}^{nD}(eV) - j_{\downarrow}^{nD}(eV)}{j_{\uparrow}^{nD}(eV) + j_{\downarrow}^{nD}(eV)} \quad (2.27)$$

$P_{G(I)}^{nD}$  measures the relative difference in the conductances (current) of opposite spin orientations in n-dimensional system. In the next section, the dependence on the dimensionality of the system and the strength of the spin-flip scattering of the total conductance and spin polarization of conductance will be examined.

## 2.3 Results and discussion

We now show and discuss the the dimensionality and the interfacial scattering effect on the total conductance and the spin polarization of conductance spectra of a M/F junction. Because we only focus on the above mentioned effects, we keep the following parameters:  $E_0$ ,  $\eta$ , and  $E_F$ , fixed throughout this section. As mentioned in the previous section, the choice of  $E_0$  only affects the shift of the spectra along the energy axis. Thus, in order to see the feature in both total conductance and

spin polarization of conductance spectra when positive voltage is applied, we set  $E_0 = E_{ex}$ . This setting makes the spectra of the conductance and spin polarization of conductance start at zero applied voltage.

The value of the ratio of the electron effective masses in the two materials  $\eta$ , and that of the Fermi energy of the metal  $E_F$ , affect the mismatch of the electron group velocities. Changing their values are expected to cause the same effect as changing the strength of the non-spin flip interface scattering (Blonder and Tinkham, 1983), which is parameterized by  $Z_0$ . So, we set  $\eta = 1$  and  $E_F = 10E_{ex}$  for the purpose of illustration in all plots. We first show the results related to the total conductance and later the spin polarization of conductance.

### 2.3.1 Total conductance

The conductance is in units of  $e^2/h$  in all relevant plots. First, we consider the dimensional effect on the total conductance spectrum. The spectrum and its derivative in each dimensional case are shown in Figure 2.2, for zero spin-flip non-spin-flip scattering:  $Z_f = Z_0 = 0$ . The total conductance spectrum is suppressed, when these two parameters are not zero, but its shape does not change much.

In all dimensional cases, the total conductance spectrum and its derivative starts at zero applied voltage, which is the position equivalent to the bottom of the spin up band of the ferromagnetic material. As the applied voltage is increased, the total conductance is also increased at a different rate in different dimensional systems. However, in all cases, there is a change in the slope of the total conductance spectrum at the applied potential energy  $eV = 2E_{ex}$ , which is equivalent to the bottom of the spin down band of the ferromagnetic material. As can be seen in Figure 2.2, this change in slope is the most prominent in 1D spectrum and least prominent in 3D spectrum. One can see a more prominent feature at this energy in the differential conductance spectrum plots for all dimensional cases.

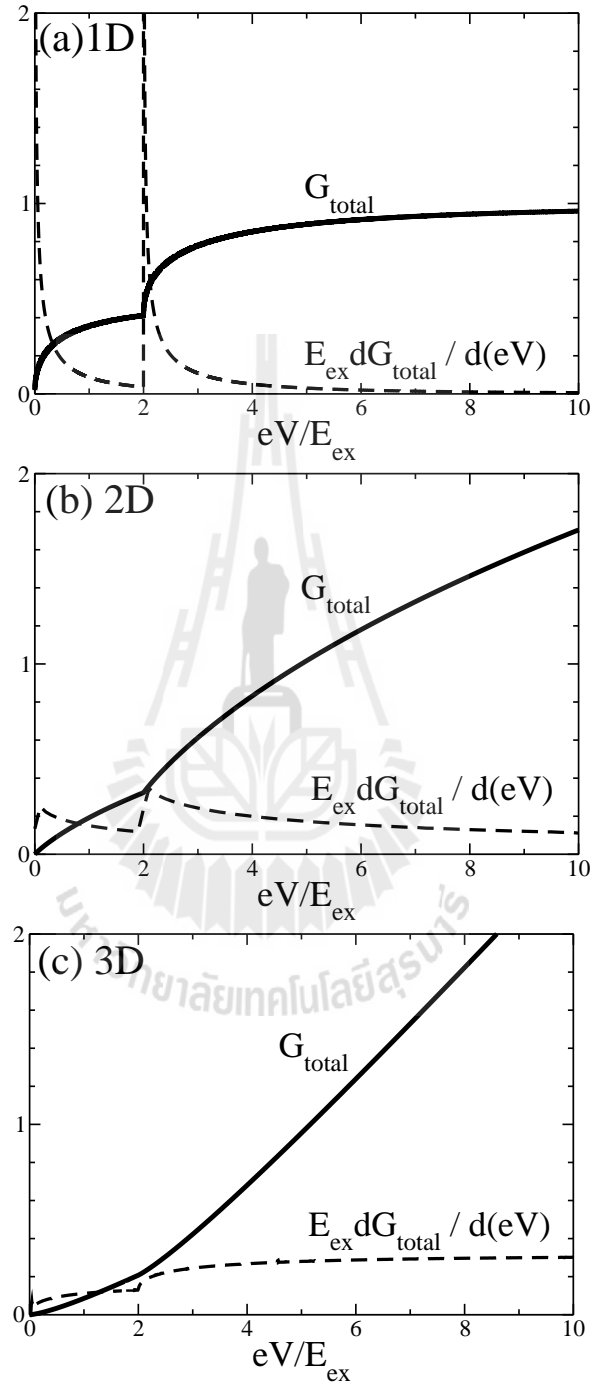


**Figure 2.2** Plots of total conductance spectra  $G_{total}$  (solid curves) and their corresponding derivatives  $E_{ex}[dG_{total}/d(eV)]$  (dashed curves) in (a) 1D, (b) 2D, and (c) 3D system.  $Z_0$  and  $Z_f$  are set to be zero.

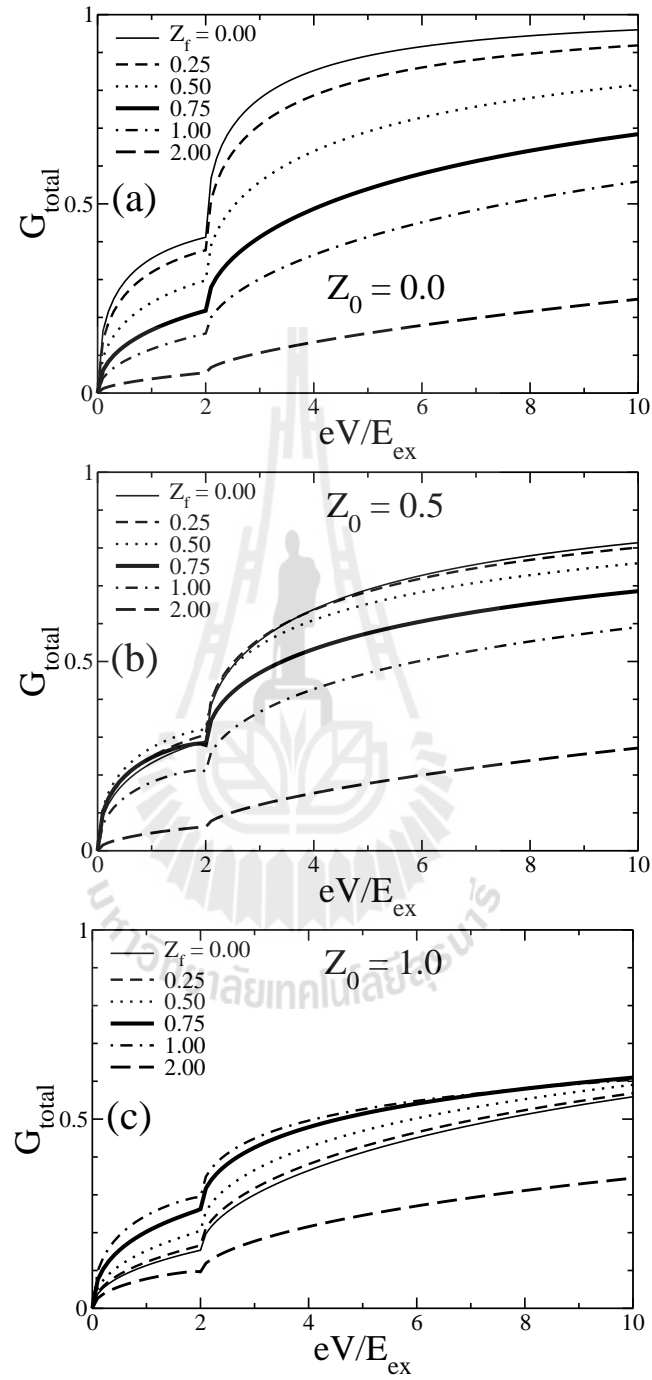


**Figure 2.3** Plots of 1D total conductance spectra  $G_{total}^{1D}$  as a function of applied potential energy  $eV$ .  $0 \leq Z_f \leq 2$ . In (a),  $Z_0 = 0.0$ , in (b),  $Z_0 = 0.5$ , and in (c),  $Z_0 = 1.0$ .

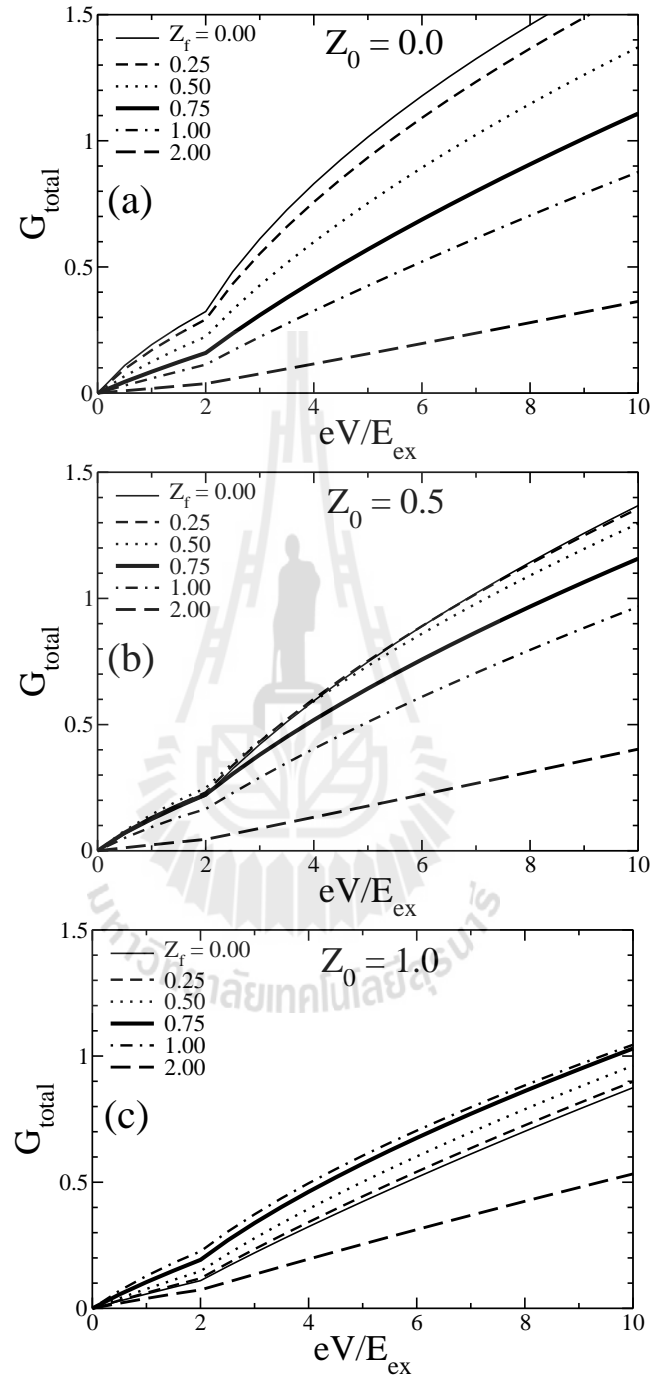


**Figure 2.4** Plots of 2D total conductance spectra  $G_{total}^{1D}$  as a function of applied potential energy  $eV$ .  $0 \leq Z_f \leq 2$  for three different values of the parameter  $Z_0$ . In (a),  $Z_0 = 0.0$ , in (b),  $Z_0 = 0.5$ , and in (c),  $Z_0 = 1.0$ .

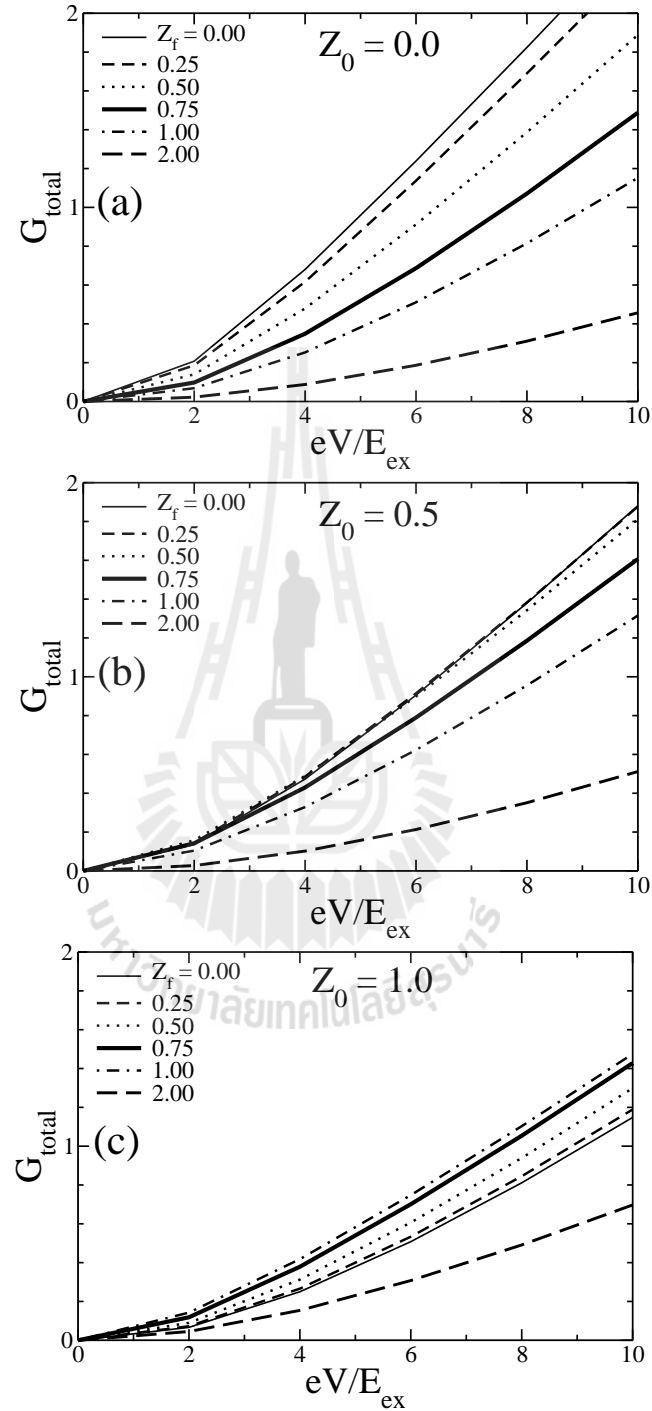


**Figure 2.5** Plots of 3D total conductance spectra  $G_{total}^{1D}$  as a function of applied potential energy  $eV$ .  $0 \leq Z_f \leq 2$  for three different values of the parameter  $Z_0$ . In (a),  $Z_0 = 0.0$ , in (b),  $Z_0 = 0.5$ , and in (c),  $Z_0 = 1.0$ .

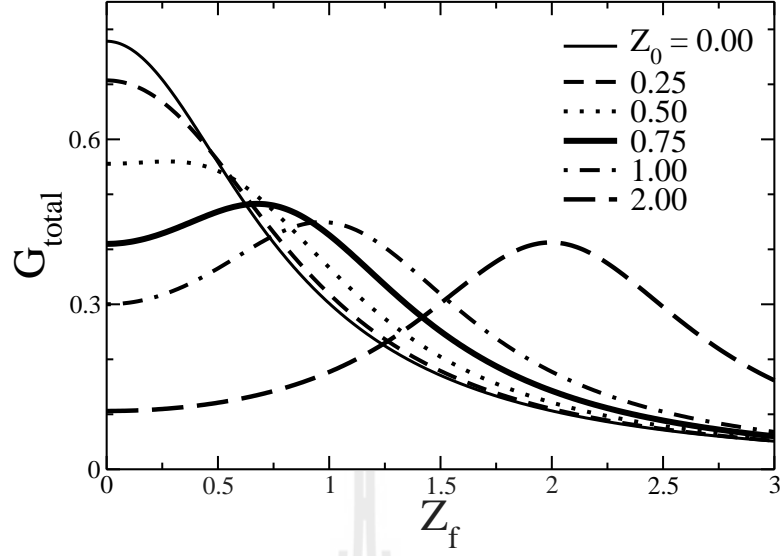


**Figure 2.6** Plots of 1D total conductance spectra  $G_{total}^{1D}$  at  $eV = 3E_{ex}$  as a function of spin-flip scattering strength parameter  $Z_f$  for various values of spin-flip scattering strength parameter  $Z_0$ .

In addition to the change in slope at  $eV = 2E_{ex}$ , the dimensionality of the system also affects the slope of the conductance spectrum at large applied voltage. Because  $k_{\uparrow\downarrow}$  and  $q$  are almost unchanged at large energy, the transmission probability  $T_{k\sigma}$  is weakly dependent of energy at large energy. Thus, following Eq. 2.21, 2.23, and 2.25, for large  $eV$  we have

$$G_{total}^{nD}(eV) \sim (eV)^{\frac{n-1}{2}} \Rightarrow \frac{dG_{total}^{nD}(eV)}{d(eV)} \sim \frac{n-1}{2}(eV)^{\frac{n-3}{2}} \quad (2.28)$$

That is,  $G_{total}^{1D}$  converges to a constant,  $G_{total}^{2D} \sim (eV)^{1/2}$ , and  $G_{total}^{3D} \sim (eV)^1$ .

Let us now consider the interfacial scattering effect. The presence of either type of interfacial scattering generally reduces the value of the total conductance. These behaviors are similar in all dimensional systems. We show the plots of total conductance with different values of  $Z_0$  and  $Z_f$  in case of 1D, 2D, and 3D M/F junctions in Figure 2.3 - 2.5, respectively. The value of  $Z_0$  determines whether the junction behavior is in the metallic (high transmission) or tunneling (low transmission) regime. The change of the total conductance spectrum in the presence of

the interfacial spin-flip scattering varies with the junction behavior. In the metallic regime:  $Z_0 \leq 0.5$ , the increase in  $Z_f$  suppresses the total conductance spectrum. In the intermediate regime:  $Z_0 \approx 0.5$ , small increase in  $Z_f$  from zero does not change  $G_{total}^{nD}$  much, but once  $Z_f \geq Z_0$ ,  $G_{total}^{nD}$  starts to decrease with  $Z_f$ . On the contrary, in the tunneling regime:  $Z_0 > 0.5$ , the increase in  $Z_f$  surprisingly enhances the total conductance spectrum until it reaches its maximum value, when  $Z_f \approx Z_0$ . When  $Z_f > Z_0$ , the conductance spectrum is suppressed. Here, we only show, in Figure 2.6, the plots of the 1D total conductance at  $eV = 3E_{ex}$  as a function of the parameter  $Z_f$  to illustrate the above mentioned fact. The results in higher dimensional systems or at other values of  $eV$  are similar, and thus are not shown. This enhancement of the total conductance due to the interfacial spin-flip scattering in the tunneling regime was also predicted to happen in metal/Rashba system junction (Srisongmuang et al., 2008).

### 2.3.2 Spin polarization of conductance and current

Let us now consider the spin polarization of conductance  $P_G^{nD}$  and current  $P_I^{nD}$  to see how relative difference in spin-up and spin-down conductances is affected by the dimensionality and interfacial scattering. The plots of  $P_{G(I)}^{nD}(eV)$  in three cases of dimensionality are shown in Figure 2.7 - 2.8. In these figures,  $Z_0$  is set to zero (metallic regime), and  $Z_f$  is varied from 0 to 2. Due to the fact that there are only electrons with spin-up when the energy is less than  $E_{ex}$ ,  $P_{G(I)}^{nD}(eV \leq E_{ex})$  is equal to one as expected. When the energy is great than  $E_{ex}$ , electrons with both types of spin exist and  $P_{G(I)}^{nD}(eV > E_{ex})$  is less than one and is decreased with the applied voltage indicating that the number of spin-up and spin-down electrons are closer to each other at higher energies. It is also noticeable that as the applied voltage increases,  $P_{G(I)}^{1D}(eV)$  approaches zero faster than  $P_{G(I)}^{2D}(eV)$  and  $P_{G(I)}^{3D}(eV)$ . From the  $P_{G(I)}^{nD}$  spectra in Figure 2.7 - 2.8, we can also see that increase in  $Z_f$  can enhance

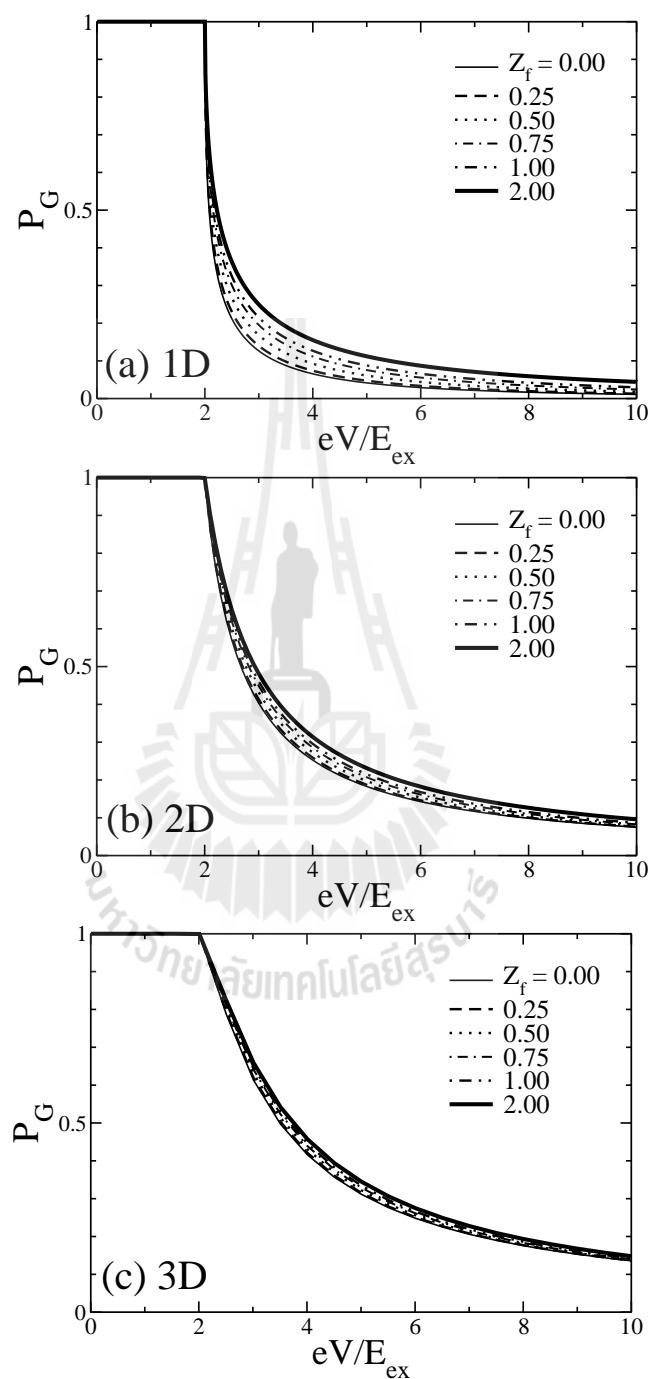


**Figure 2.7** Plots of spin polarization of conductance spectra as a function of applied potential energy  $eV$  in (a) 1D, (b) 2D, and (c) 3D system for  $Z_0 = 0$  and  $0 \leq Z_f \leq 2$ .

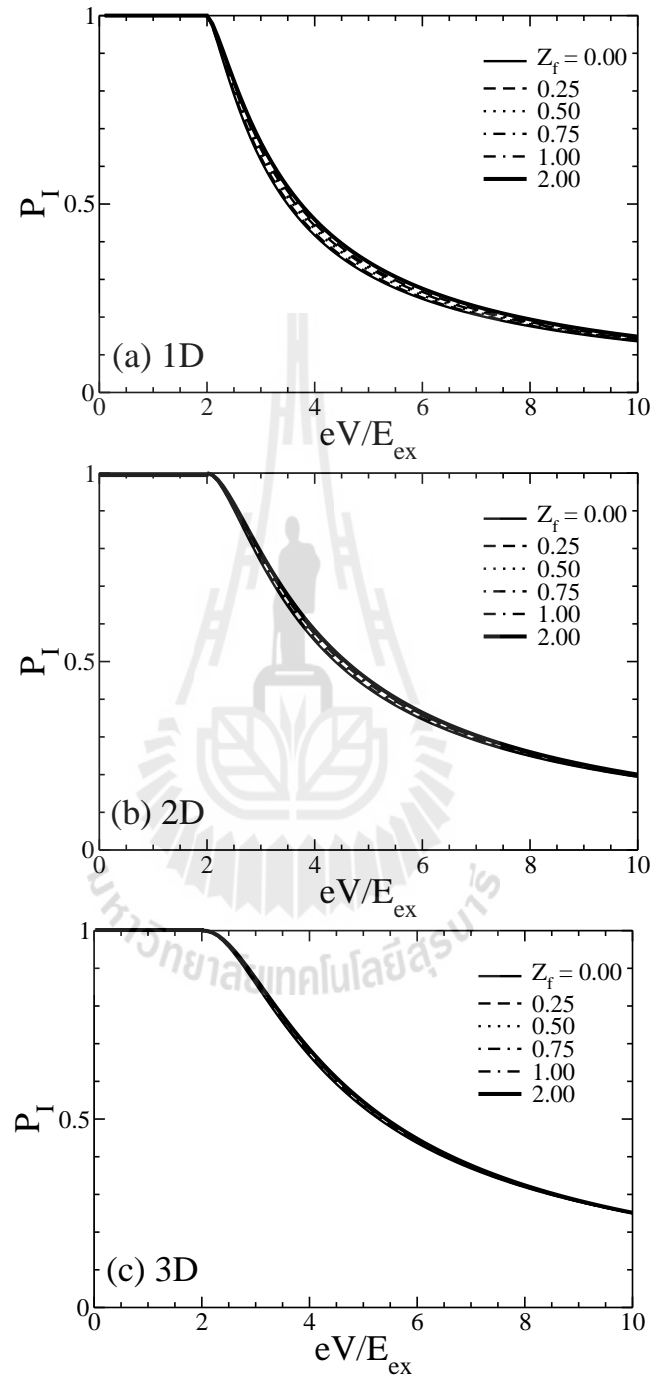


**Figure 2.8** Plots of spin polarization of current as a function of applied potential energy  $eV$  in (a) 1D, (b) 2D, and (c) 3D system for  $Z_0 = 0$  and  $0 \leq Z_f \leq 2$ .

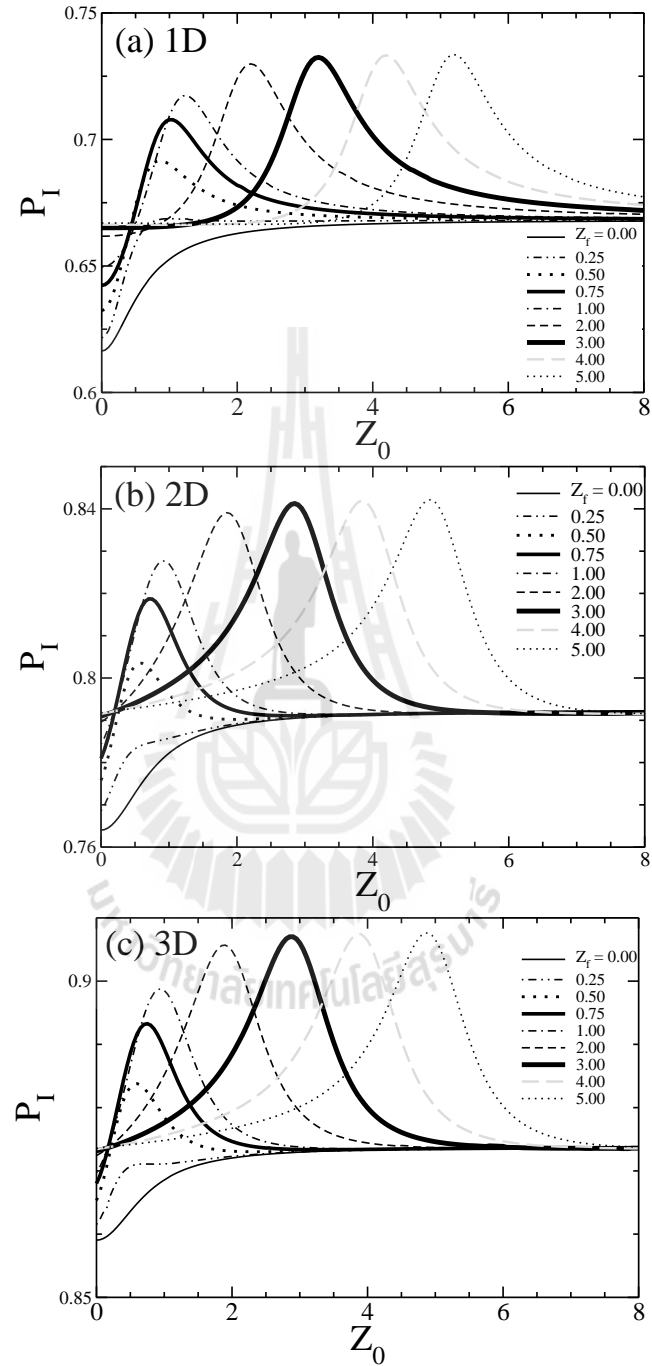


**Figure 2.9** Plots of spin polarization of current  $P_I^{nD}$  as a function of potential strength  $Z_0$  in (a) 1D, (b) 2D, and (c) 3D system for various the spin-flip scattering  $0 \leq Z_f \leq 5$ .

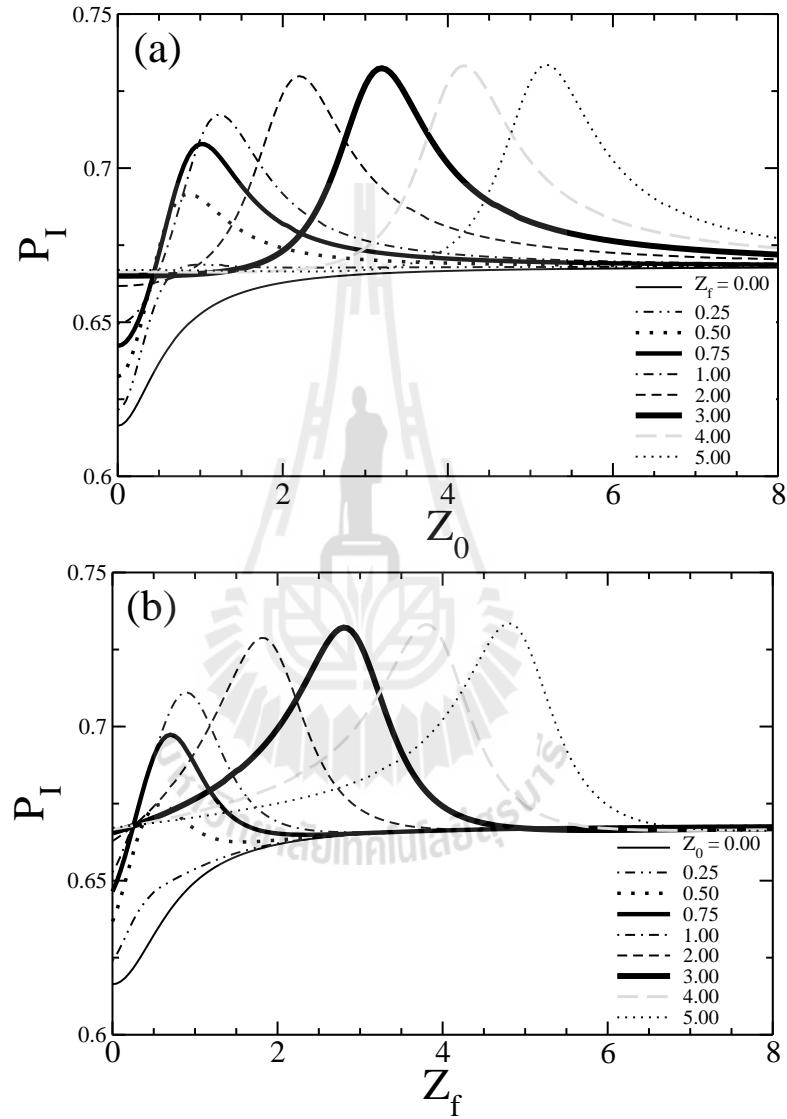


**Figure 2.10** Plots of 1D spin polarization of current  $P_I^{nD}$  as a function of (a) potential strength  $Z_0$  and  $0 \leq Z_f \leq 5$  and (b) spin-flip scattering  $Z_f$  and  $0 \leq Z_0 \leq 5$ .

$P^{nD}(eV > E_{ex})$ . This enhancement is strongest in 1D system and weakest in 3D system.

The effect of the interfacial scattering on  $P_I^{nD}$  can be seen more clearly in Figure 2.9. We chose to plot  $P^{nD}(eV = 3E_{ex})$  as a function of  $Z_f$  at various value of  $Z_0$ . The plots of  $P^{nD}(eV)$  at other values of  $eV$  as a function of  $Z_f$  show similar dependence on  $Z_f$ . In 1D case, in the metallic and intermediate regime the presence of  $Z_f$  enhances  $P^{1D}$ . When  $Z_f \rightarrow \infty$ , it reaches its maximum values

$$P_{\max}^{nD}(E) = \frac{k_{\uparrow}(E) - k_{\downarrow}(E)}{k_{\uparrow}(E) + k_{\downarrow}(E)} \quad (2.29)$$

independent of  $Z_0$ . The increase with  $Z_f$  does not happen in the tunneling limit. The presence the spin-flip scattering does not affect  $P^{1D}$  much. Its value is already close to  $P^{1D}$  max even when  $Z_f$  is small.

Things are somewhat different in 2D and 3D systems. In the metallic regime,  $P^{2D}(eV)$  and  $P^{3D}(eV)$  behave similarly to  $P^{1D}(eV)$ . That is, they are increased with  $Z_f$  to a maximum value, as  $Z_f$  approaches infinity. However, in the intermediate and tunneling limit,  $P^{2D}(eV)$  and  $P^{3D}(eV)$  is increased with  $Z_f$  until they reaches a maximum at  $Z_f \approx Z_0$  and then is decreased with  $Z_f$  to a value at  $Z_f \rightarrow \infty$ :

$$P_{\max}^{2D,3D}(E) = \frac{\langle k_{\uparrow}(E) \rangle - \langle k_{\downarrow}(E) \rangle}{\langle k_{\uparrow}(E) \rangle + \langle k_{\downarrow}(E) \rangle}, \quad (2.30)$$

where  $\langle f \rangle$  is the average over angle or solid angle of  $f$  in 2D and 3D system. Surprisingly, this maximum at  $Z_f \approx Z_0$  in the spin polarization of conductance does not happen in 1D system, because  $G_{\uparrow}^{1D} - G_{\downarrow}^{1D}$  is relatively much lower than  $G_{\uparrow}^{1D} + G_{\downarrow}^{1D}$  in comparison to those in higher dimensional systems but this maximum value does happens in the spin polarization of current as shown in Figure 2.9.

## 2.4 Conclusions

We have considered the effect of dimensionality and interfacial scattering, including spin-flip scattering, on the the total conductance and spin polarization of conductance of M/F junction. The total conductance spectrum of M/F junction in 1D system contains sharpest feature at the energy equivalent to the bottom of the minority band. The presence of interfacial scattering generally suppresses the total conductance spectra in all dimensional cases. However, there is a special circumstance, like in the tunneling limit, in which the total conductance can be enhanced by the presence of the interfacial spin-flip scattering, and a maximum value of total conductance can be reached, when the strength of the non-spin-flip and spin-flip scattering are equal. This enhancement happens in all dimensional systems.

As expected, the value of spin polarization of conductance is equal to one in all energies between the bottoms of the two bands of the ferromagnetic material, and is decreased as the energy becomes higher than the bottom of the minority band. This decrease is more rapidly in 1D than in 2D and 3D systems. Also, the value of the spin polarization of conductance is larger in 1D than in 2D and 3D system.

In 1D junction in the metallic regime, the interfacial spin-flip scattering enhances the spin polarization of conductance and current to a maximum value. In the tunneling regime, the spin polarization of conductance and current is close to this maximum even when the strength of the spin-flip scattering is negligible. The increase in the strength of this scattering does not affect the spin polarization of conductance and current in this limit. In 2D and 3D junctions, the behavior of the spin polarization of conductance and current in the metallic regime is similar to that in 1D junctions, but in the tunneling limit its value can reach to a different maximum when the strength of the non-spin-flip and spin-flip scattering are equal. This maximum is higher than the maximum value in the metallic regime.

# CHAPTER III

## ELECTRONIC PROPERTIES OF FERROMAGNET WITHIN A TWO-BAND MODEL

### 3.1 s-d band coupling Hamiltonian

From the band structure calculations of ferromagnetic material, there are the hybridization regions between the s band and the d band near Fermi level. In principle, this scenario is caused by a mixing or overlap of the wave functions of electron with spin-up and spin-down from both bands. Because of this reason, we consider the kinetic energy of valence electrons with spin-up and spin-down from both bands (the s band and the d band) via the coupling strength  $t$ . The Hamiltonian in this case is

$$H_{FM} = \begin{bmatrix} \xi_{\uparrow}^d(k) & 0 & t_{\uparrow\uparrow} & t_{\uparrow\downarrow} \\ 0 & \xi_{\downarrow}^d(k) & t_{\downarrow\uparrow} & t_{\downarrow\downarrow} \\ t_{\uparrow\uparrow} & t_{\downarrow\uparrow} & \xi_{\uparrow}^s(k) & 0 \\ t_{\uparrow\downarrow} & t_{\downarrow\downarrow} & 0 & \xi_{\downarrow}^s(k) \end{bmatrix}, \quad (3.1)$$

where  $\xi_{\sigma}^{s(d)}(k)$  is the kinetic energy of electron in the s(d) band, and with spin  $\sigma$  configuration.  $t_{\uparrow\uparrow(\downarrow\downarrow)}$  is the coupling strength between spin-up (down) electrons from the s band and the d band,  $t_{\uparrow\downarrow(\downarrow\uparrow)}$  is the coupling strength between opposite-spin electrons from the s band and the d band.

We assume that the mixing between the different spin configurations from different bands is zero ( $t_{\uparrow\downarrow}$  and  $t_{\downarrow\uparrow} = 0$ ). We set  $t_{\uparrow\uparrow} = t_{\downarrow\downarrow} = t$  because there is no any evidence that confirms which coupling is more dominated. Also, Coulomb

interaction (charge interaction) is neglected in this thesis. Thus, the Hamiltonian in Eq. 3.1 becomes

$$H_{FM} = \begin{bmatrix} \xi_{\uparrow}^d(k) & 0 & t & 0 \\ 0 & \xi_{\downarrow}^d(k) & 0 & t \\ t & 0 & \xi_{\uparrow}^s(k) & 0 \\ 0 & t & 0 & \xi_{\downarrow}^s(k) \end{bmatrix}, \quad (3.2)$$

where the energy dispersions in each band within a free electron approximation in this model are given by equations below.

$$\xi_{\uparrow}^d(k) = \frac{\hbar^2 k^2}{2m_d^*} - E_{ex}^d - E_{F-\uparrow}^d, \quad (3.3)$$

$$\xi_{\downarrow}^d(k) = \frac{\hbar^2 k^2}{2m_d^*} + E_{ex}^d - E_{F-\downarrow}^d, \quad (3.4)$$

$$\xi_{\uparrow}^s(k) = \frac{\hbar^2 k^2}{2m_s^*} - E_{ex}^s - E_{F-\uparrow}^s, \quad (3.5)$$

$$\xi_{\downarrow}^s(k) = \frac{\hbar^2 k^2}{2m_s^*} + E_{ex}^s - E_{F-\downarrow}^s, \quad (3.6)$$

where superscript s(d) refers to the s band (d band) while subscript  $\uparrow$  ( $\downarrow$ ) refers to spin-up (down) configuration. The electron effective mass in s-band is indicated by  $m_s^*$ , while  $m_d^*$  is for d-band. These two effective masses are different as can be seen in the band structure calculations. However, the electron effective mass of different spin bands in the same energy band are assumed to be equal. That is  $m_{s\uparrow}^* = m_{s\downarrow}^* = m_s^*$  and  $m_{d\uparrow}^* = m_{d\downarrow}^* = m_d^*$ . This is because the slope of energy dispersion of electron with spin-up and spin-down in either s or d-band has almost the same value. It is found from the band structure calculations that the exchange energy in s-band ( $E_{ex}^s$ ) and d-band ( $E_{ex}^d$ ) are different. Some exchange energies in ferromagnet are shown in Table 3.1. Fermi energies of electron with spin-up  $E_{F-\uparrow}^{d(s)}$  and spin-down  $E_{F-\downarrow}^{d(s)}$  bands are also different.

The dispersion relations in Equations 3.3 - 3.6 are plotted in Figure 3.1(a). In this figure, the energy bands are shifted by  $E_0$  (no Fermi level) because we want to

**Table 3.1** The exchange energies of some ferromagnetic materials.  $E_{ex}^s$  is the exchange energy in s-band, while  $E_{ex}^d$  is that in d-band. The data are taken from D. Y. Petrovykh et al. (Petrovykh et al., 1998) and J. Callaway and C. S. Wang (Callaway and Wang, 1977).

Crystal	$E_{ex}^s$ (eV)	$E_{ex}^d$ (eV)
Ni	0.23	-
Ni <sub>0.8</sub> Fe <sub>0.2</sub>	0.27	-
Fe	1.36	2.56

compare the results with those from one-band model in Chapter II. One significant thing we have seen in this figure is the crossing points between the same spin bands but different energy band dispersions ( $\xi_{\downarrow}^d$  and  $\xi_{\downarrow}^s$ ) as indicated by solid arrows. These crossing points are due to our parameters  $m_d^* \neq m_s^*$ . In particular, these crossing points can effect the electronic transport in the M/FM junction as will be seen in the next chapter.

The eigenvalues are given by

$$\lambda_{mix-\uparrow}^d(k) = \frac{\xi_{\uparrow}^d(k) + \xi_{\uparrow}^s(k)}{2} + \sqrt{\left| \frac{\xi_{\uparrow}^d(k) - \xi_{\uparrow}^s(k)}{2} \right|^2 + t^2}, \quad (3.7)$$

$$\lambda_{mix-\downarrow}^d(k) = \frac{\xi_{\downarrow}^d(k) + \xi_{\downarrow}^s(k)}{2} + \sqrt{\left| \frac{\xi_{\downarrow}^d(k) - \xi_{\downarrow}^s(k)}{2} \right|^2 + t^2}, \quad (3.8)$$

$$\lambda_{mix-\uparrow}^s(k) = \frac{\xi_{\uparrow}^d(k) + \xi_{\uparrow}^s(k)}{2} - \sqrt{\left| \frac{\xi_{\uparrow}^d(k) - \xi_{\uparrow}^s(k)}{2} \right|^2 + t^2}, \quad (3.9)$$

$$\lambda_{mix-\downarrow}^s(k) = \frac{\xi_{\downarrow}^d(k) + \xi_{\downarrow}^s(k)}{2} - \sqrt{\left| \frac{\xi_{\downarrow}^d(k) - \xi_{\downarrow}^s(k)}{2} \right|^2 + t^2}, \quad (3.10)$$

where subscript *mix* refers to the system of a hybridization (s-d mixing), so that these four equations are 4 mixing bands. We still superscript either *d* or *s* in these equations because we want to remind the reader that these 4 mixing bands can become the energy bands in the normal case (no coupling) when  $t = 0$ .

That is, when  $t = 0$ , the eigenvalues become

$$\lambda_{mix-\uparrow}^d(k) = \xi_{\uparrow}^d(k) \quad (3.11)$$

$$\lambda_{mix-\downarrow}^d(k) = \xi_{\downarrow}^d(k) \quad (3.12)$$

$$\lambda_{mix-\uparrow}^s(k) = \xi_{\uparrow}^s(k) \quad (3.13)$$

$$\lambda_{mix-\downarrow}^s(k) = \xi_{\downarrow}^s(k) \quad (3.14)$$

At  $k = 0$ , the eigenvalues are

$$\lambda_{mix-\uparrow, 0}^d = \frac{E_0^d - E_{ex}^d - E_{ex}^s + E_0^s}{2} + \sqrt{\left| \frac{E_0^d - E_{ex}^d + E_{ex}^s - E_0^s}{2} \right|^2 + t^2}, \quad (3.15)$$

$$\lambda_{mix-\downarrow, 0}^d = \frac{E_0^d + E_{ex}^d + E_{ex}^s + E_0^s}{2} + \sqrt{\left| \frac{E_0^d + E_{ex}^d - E_{ex}^s - E_0^s}{2} \right|^2 + t^2}, \quad (3.16)$$

$$\lambda_{mix-\uparrow, 0}^s = \frac{E_0^d - E_{ex}^d - E_{ex}^s + E_0^s}{2} - \sqrt{\left| \frac{E_0^d - E_{ex}^d + E_{ex}^s - E_0^s}{2} \right|^2 + t^2}, \quad (3.17)$$

$$\lambda_{mix-\downarrow, 0}^s = \frac{E_0^d + E_{ex}^d + E_{ex}^s + E_0^s}{2} - \sqrt{\left| \frac{E_0^d + E_{ex}^d - E_{ex}^s - E_0^s}{2} \right|^2 + t^2}. \quad (3.18)$$

The corresponding eigenenergies are

$$\psi_{\uparrow}^{\pm} = \frac{1}{N_{\uparrow}^{\pm}} \begin{bmatrix} -\left( \frac{\xi_{\uparrow}^d(k) - \xi_{\uparrow}^s(k) \mp \sqrt{|\xi_{\uparrow}^d(k) - \xi_{\uparrow}^s(k)|^2 + 4t^2}}{2t} \right) \\ 0 \\ 1 \\ 0 \end{bmatrix}, \quad (3.19)$$

$$\psi_{\downarrow}^{\pm} = \frac{1}{N_{\downarrow}^{\pm}} \begin{bmatrix} 0 \\ -\left( \frac{\xi_{\downarrow}^d(k) - \xi_{\downarrow}^s(k) \mp \sqrt{|\xi_{\downarrow}^d(k) - \xi_{\downarrow}^s(k)|^2 + 4t^2}}{2t} \right) \\ 0 \\ 1 \end{bmatrix}, \quad (3.20)$$

where superscript  $+(-)$  refers to the wave function of eigenvalue  $\lambda_{mix-\sigma}^{d(s)}$  band with

spin  $\sigma$ , and the normalization factors are

$$[N_{\uparrow}^{\pm}]^2 = \frac{2[\xi_{\uparrow}^d(k) - \xi_{\uparrow}^s(k)]^2 \mp 2[\xi_{\uparrow}^d(k) - \xi_{\uparrow}^s(k)]\sqrt{|\xi_{\uparrow}^d(k) - \xi_{\uparrow}^s(k)|^2 + 4t^2 + 8t^2}}{4t^2}, \quad (3.21)$$

$$[N_{\downarrow}^{\pm}]^2 = \frac{2[\xi_{\downarrow}^d(k) - \xi_{\downarrow}^s(k)]^2 \mp 2[\xi_{\downarrow}^d(k) - \xi_{\downarrow}^s(k)]\sqrt{|\xi_{\downarrow}^d(k) - \xi_{\downarrow}^s(k)|^2 + 4t^2 + 8t^2}}{4t^2}. \quad (3.22)$$

One can see from the eigenenergies that there are a mixing between the same spin configuration from different energy bands.

### 3.2 Energy dispersion relation

We now look more closely at the energy dispersion relation for each band. We start by considering the definition of the electron effective mass  $m^*$  in the crystal within the free electron approximation model. The electron effective mass is defined by

$$\frac{1}{m^*} = \frac{1}{\hbar^2} \frac{d^2 E}{dk^2}, \quad (3.23)$$

where  $E = E(k)$  is the energy dispersion relation. That is, the electron effective mass is inversely proportional to the curvature of the energy dispersion relation. In the band structure picture, the effective mass of the d band is larger than that of the s band:  $m_d^* > m_s^*$ . The electron and hole effective masses  $m_e^*$  and  $m_h^*$  in some materials are shown in Table 3.2.

In Figure 3.1, the energy dispersion relations of four mixed bands are shown in the case where (a)  $t = 0$  and (b)  $t = 0.05$  eV, respectively. Clearly, the figure shows the two kinds of the crossing points between bands. That is, in Figure 3.1(a) the crossing points between the same spin direction from different bands are indicated by the solid arrows, while the dashed arrows indicate the crossing points between the

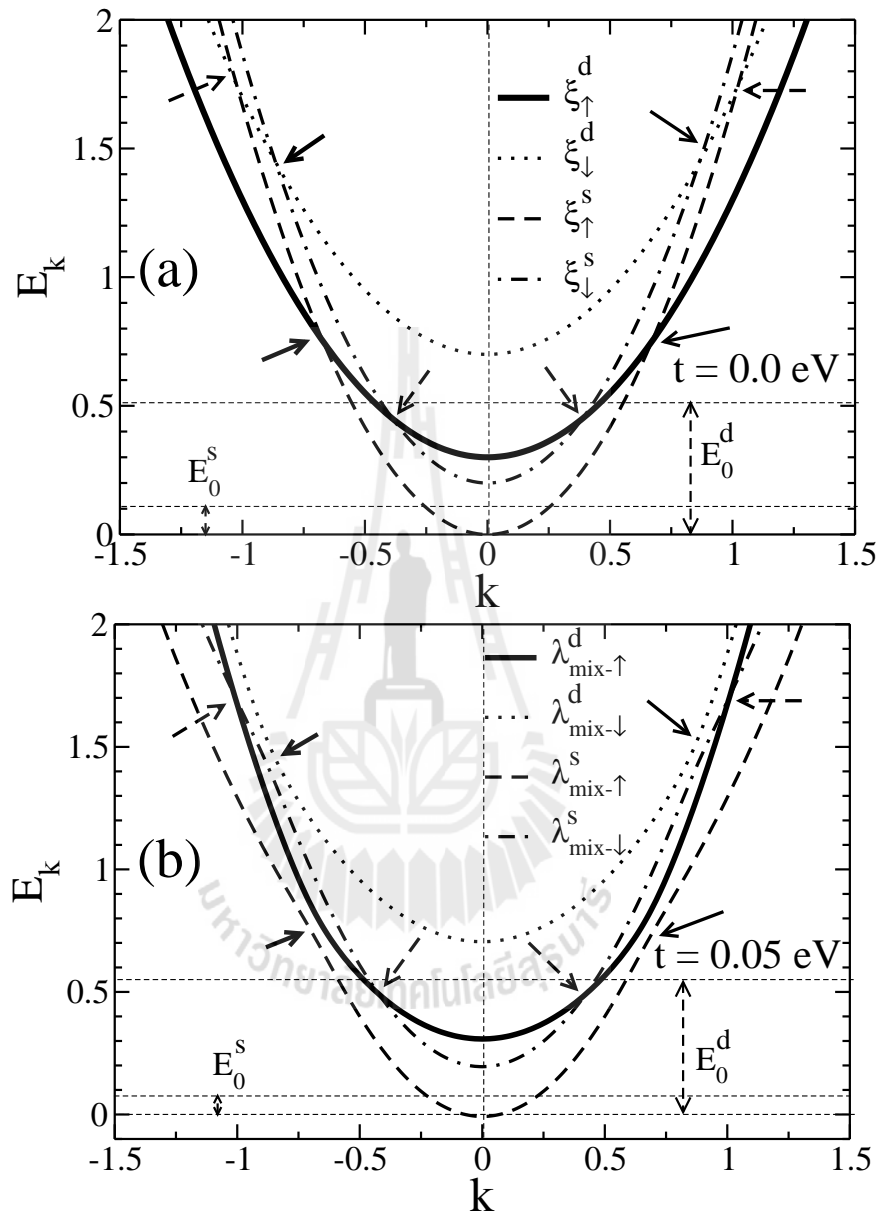


**Figure 3.1** Energy dispersion relations of ferromagnet in a two-band model. In these plots, we take  $E_{ex}^d = 0.2$  eV,  $E_{ex}^s = 0.1$  eV,  $E_0^s = 0.1$  eV,  $E_0^d = 0.5$  eV, and the electron effective masses in d-band and s-band are  $m_d^* = 0.5m_e$  and  $m_s^* = 0.3m_e$ , respectively, where  $m_e$  is electron mass. The coupling between the same spin bands are taken to be (a)  $t = 0$  eV, and (b)  $t = 0.05$  eV. In (a), the crossing points occur at different energy bands as indicated by arrows. In (b), the corresponding avoiding crossing points are indicated by solid arrows.

**Table 3.2** The electron  $m_e^*$  and hole  $m_h^*$  effective masses in direct band gap semiconductors and some ferromagnets. The data are taken from Introduction to solid state physics (Kittel, 2005).

Crystal	Electron ( $m_e^*/m_e$ )	Heavy hole ( $m_h^*/m_h$ )	Light hole ( $m_h^*/m_h$ )
InSb	0.015	0.39	0.021
InAs	0.026	0.41	0.025
InP	0.073	0.4	0.078
GaSb	0.047	0.3	0.06
GaAs	0.066	0.5	0.082
Cu <sub>2</sub> O	0.99	-	0.58
Fe	1	-	-

**Table 3.3** Carrier mobilities at room temperature of some materials, in  $cm^2/V - s$ . The data is taken from Introduction to solid state physics (Kittel, 2005).

Crystal	Electrons	Holes	Crystal	Electrons	Holes
Diamond	1800	1200	GaAs	8000	300
Si	1350	480	GaSb	5000	1000
Ge	3600	1800	PbS	550	600
InSb	800	450	PbSe	1020	930
InAs	30000	450	PbTe	2500	1000
InP	4500	100	AgCl	50	-
AlAs	280	-	KBr(100 K)	100	-
AlSb	900	400	SiC	100	10-20

bands with the opposite spin directions. When  $t$  is present as shown in Figure 3.1(b) the crossing points in the first case are affected by this  $t$ , and are opened up, whereas the crossing points in the second case still cross.

As  $t$  increases, the gaps opened at the first kind of crossing points become larger, as can be seen in Figure 3.2(a) and (c). However, the crossing points between the bands of the opposite spin directions still cross.

### 3.3 Density of states

In this section, we show the density of states of electron in the ferromagnet in two-band model. By definition (Marder, 2000), the density of states is

$$\rho^D(\varepsilon) = \left(\frac{L}{2\pi}\right)^D \int_{-\infty}^{\infty} d\mathbf{k} \delta(\varepsilon - \varepsilon_{\mathbf{k}}) \quad (3.24)$$

where index  $D$  refers to dimension of the system.  $d\mathbf{k}$  is  $dk_x$  for 1D system,  $dk_x dk_y$  for 2D system,  $dk_x dk_y dk_z$  for 3D system in cartesian coordinate.  $\delta(\varepsilon - \varepsilon_{\mathbf{k}})$  is Dirac delta function. Our main interest is the effect of the coupling strength on the DOS. However, before we show the results of the density of states in the two-band model, we will discuss those in the one-band model first.

#### 3.3.1 DOS in the one-band model

The DOS depends on the dimensionality of the system. By using Eq. 3.24, the DOS in 1D, 2D, and 3D systems are

$$\rho_{\uparrow(\downarrow)}^{1D}(\varepsilon) \propto \frac{1}{\sqrt{E \mp E_{ex}}}, \quad (3.25)$$

$$\rho_{\uparrow(\downarrow)}^{2D}(\varepsilon) \propto \text{constant}, \quad (3.26)$$

$$\rho_{\uparrow(\downarrow)}^{3D}(\varepsilon) \propto \sqrt{E \mp E_{ex}}, \quad (3.27)$$

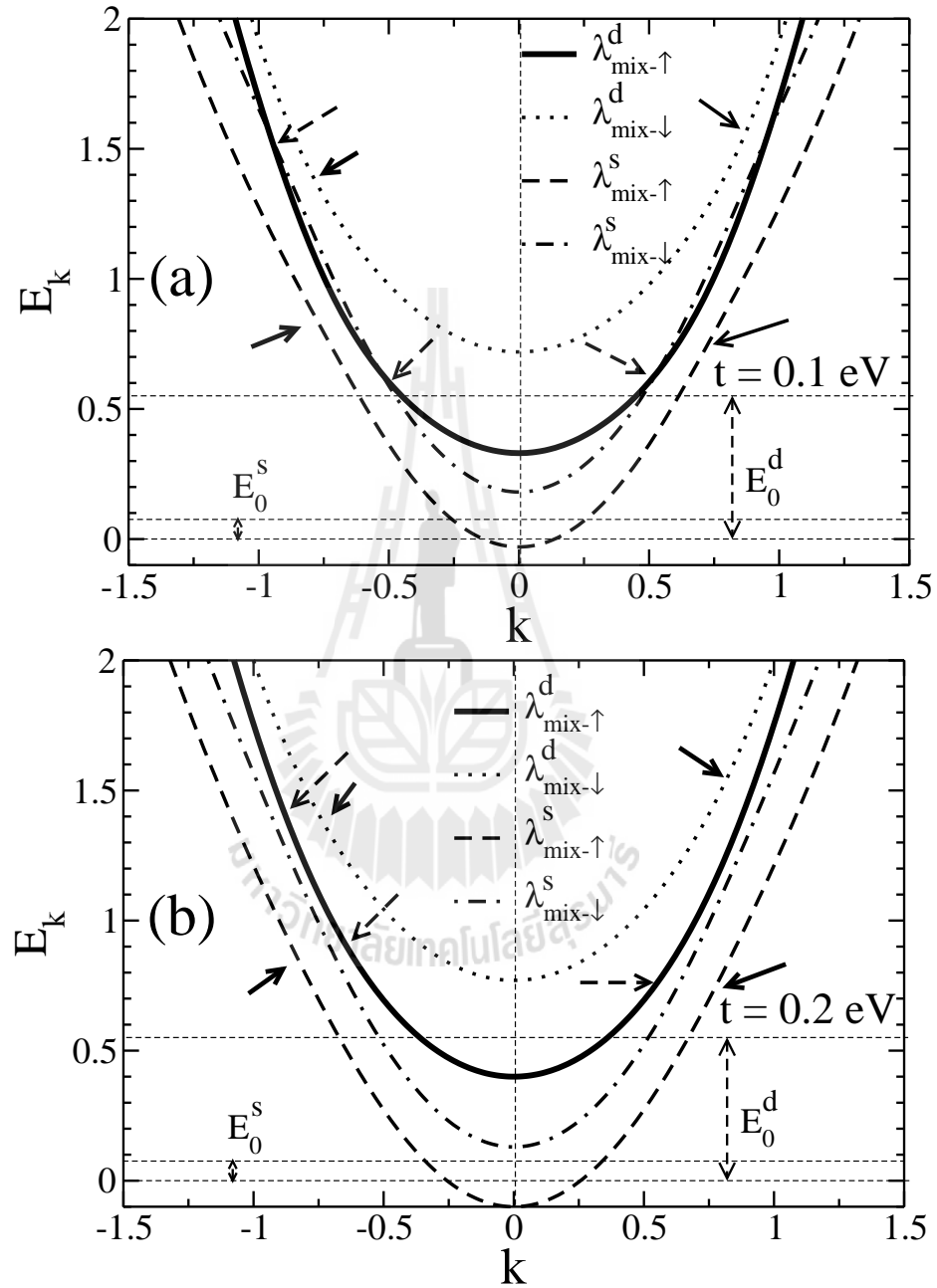


**Figure 3.2** Energy dispersion relations of two-band ferromagnet. The exchange energies and the effective mass of s and d-band are the same as in Figure 3.1. In (a)  $t = 0.1 \text{ eV}$  and (b)  $t = 0.2 \text{ eV}$ .

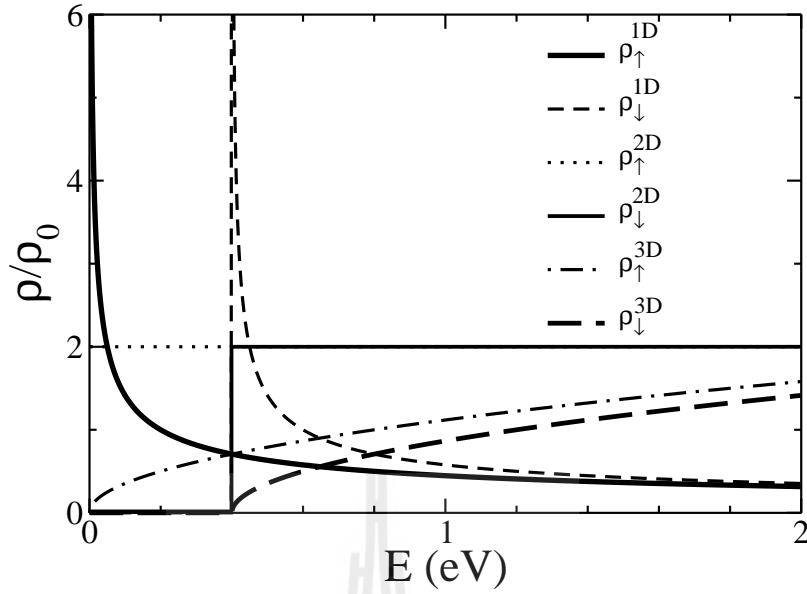


**Figure 3.3** Density of states in one-band model.  $E_{ex} = 0.2 \text{ eV}$ ,  $\rho_0$  are  $\sqrt{m^*/8\pi^2\hbar^2}$ ,  $m^*/4\pi\hbar^2$ , and  $\sqrt{2m^{*3}/4\pi^4\hbar^6}$  for 1D, 2D, and 3D system respectively.

### 3.3.2 DOS in the two-band model

In this section, we will consider the density of states of ferromagnet in the two-band model.

#### Case I: $t = 0$

In this case, the DOS is still calculated from Equation 3.24. We set  $m_e$  and  $\hbar$  to be 1, for simplicity. Other parameters such as  $E_{ex}^s$ ,  $E_{ex}^d$ ,  $E_0$ ,  $m_d^*$ ,  $m_s^*$ , and  $t$  are set to be similar to those in experiments.

In Figure 3.4, the DOS of a ferromagnet in the two-band model in 1D, 2D, and 3D system are shown when  $t = 0$ . It is found that the DOS in this case is the same as that in the one-band model as shown in Figure 3.3. Because there are two energy bands, the crossing points between bands occur. Again, there are two kinds of these crossing points as mentioned in the previous section. That is, the first kind of the crossing points occur between the bands with the same spin direction. The second kind of the crossing points occur between the bands with spin in opposite direction.

#### Case II: $t \neq 0$

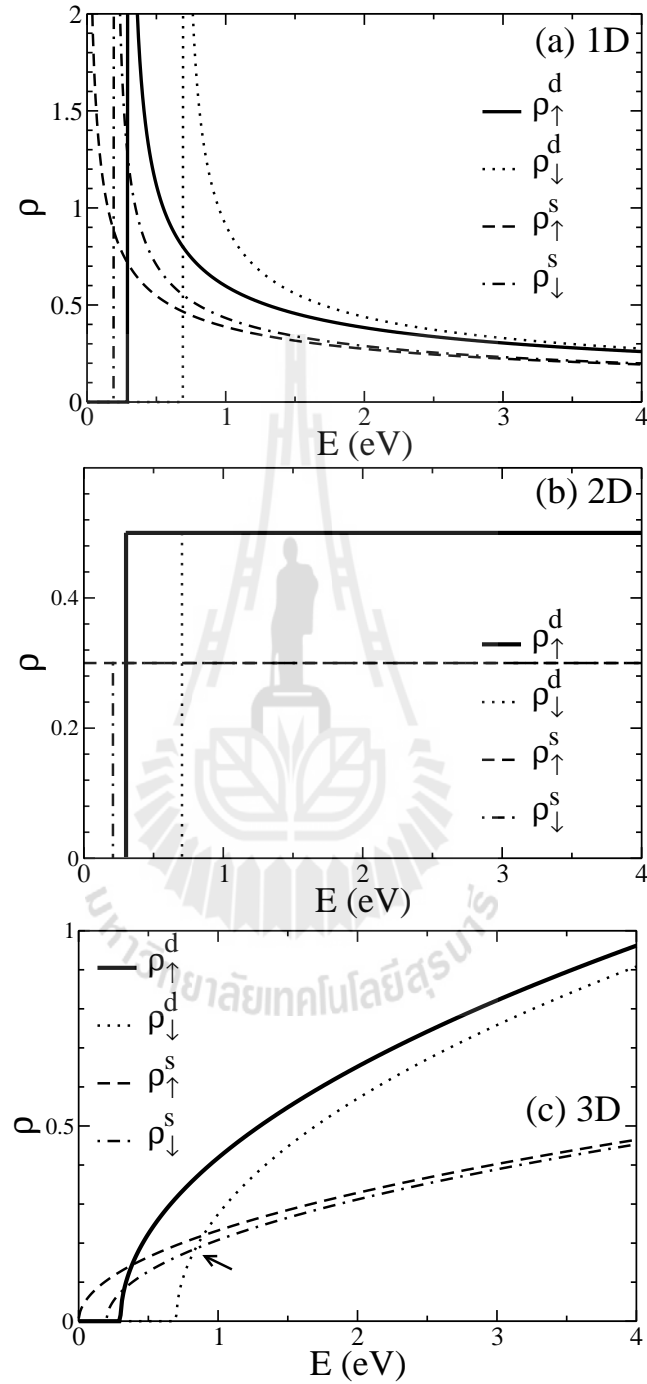


**Figure 3.4** The DOS of two-band ferromagnet when  $t = 0$  are plotted for (a) 1D, (b) 2D, and (c) 3D system. Parameters are for  $E_{ex}^d = 0.2$  eV,  $E_{ex}^s = 0.1$  eV,  $E_0^s = 0.1$  eV,  $E_0^d = 0.5$  eV,  $m_d^* = 0.5m_e$  and  $m_s^* = 0.3m_e$ , respectively, where  $m_e$  is electron mass.

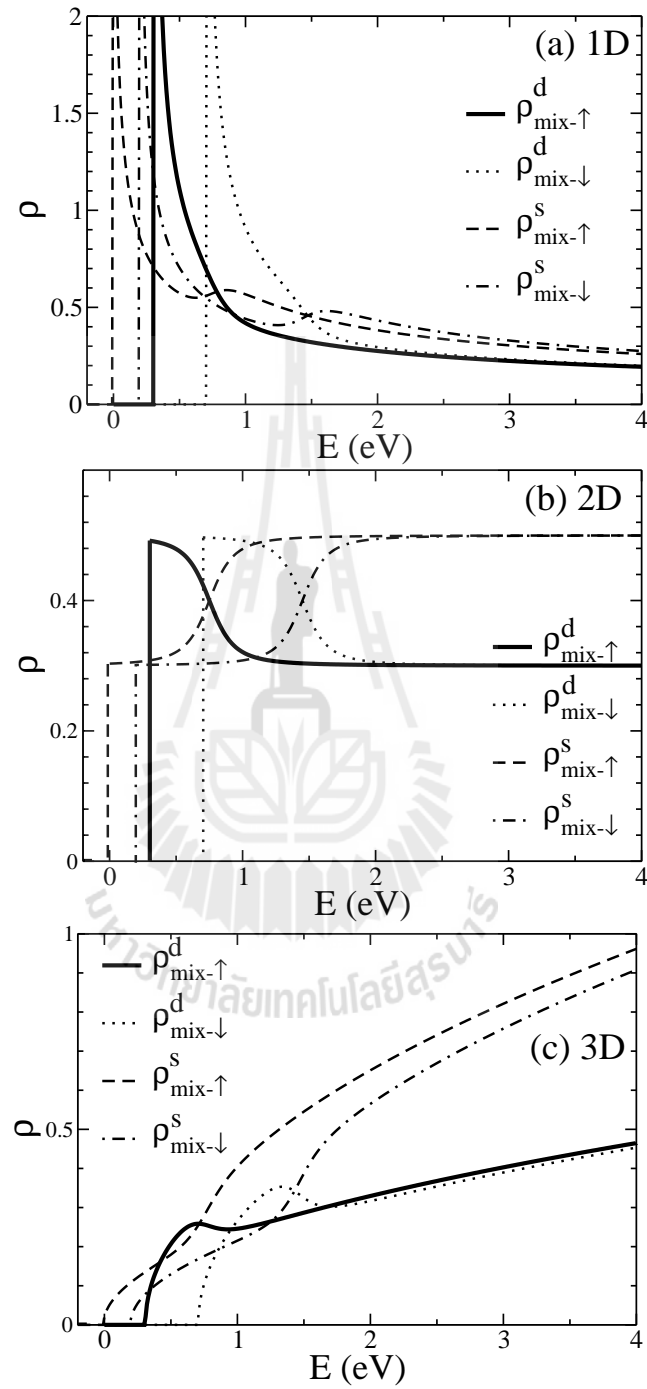


**Figure 3.5** The DOS of two-band system are plotted for (a) 1D, (b) 2D, and (c) 3D systems. The exchange energies and the electron effective masses are the same as in Figure 3.4, but  $t = 0.05$  eV. Subscript *mix* refers to s-d mixing system.

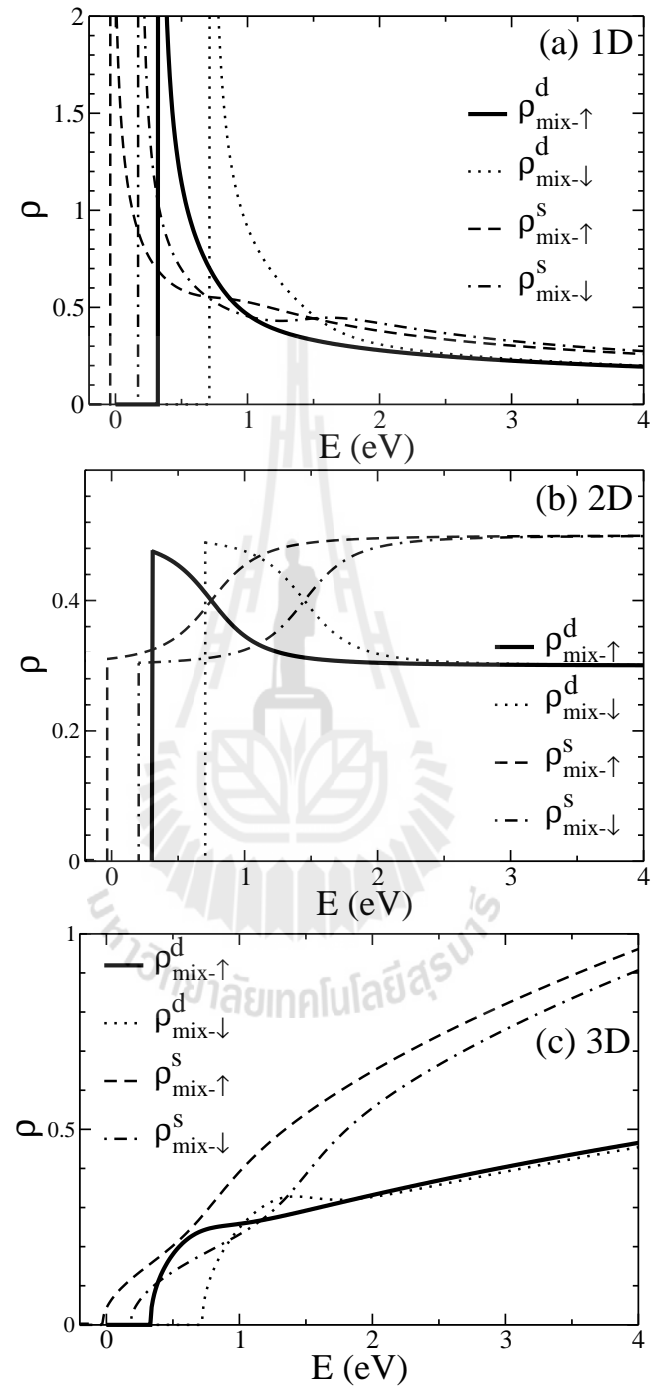


**Figure 3.6** The DOS of two-bands ferromagnet are plotted for (a) 1D, (b) 2D, and (c) 3D systems. The exchange energies and the electron effective masses are the same as in Figure 3.4, but  $t = 0.1$  eV.

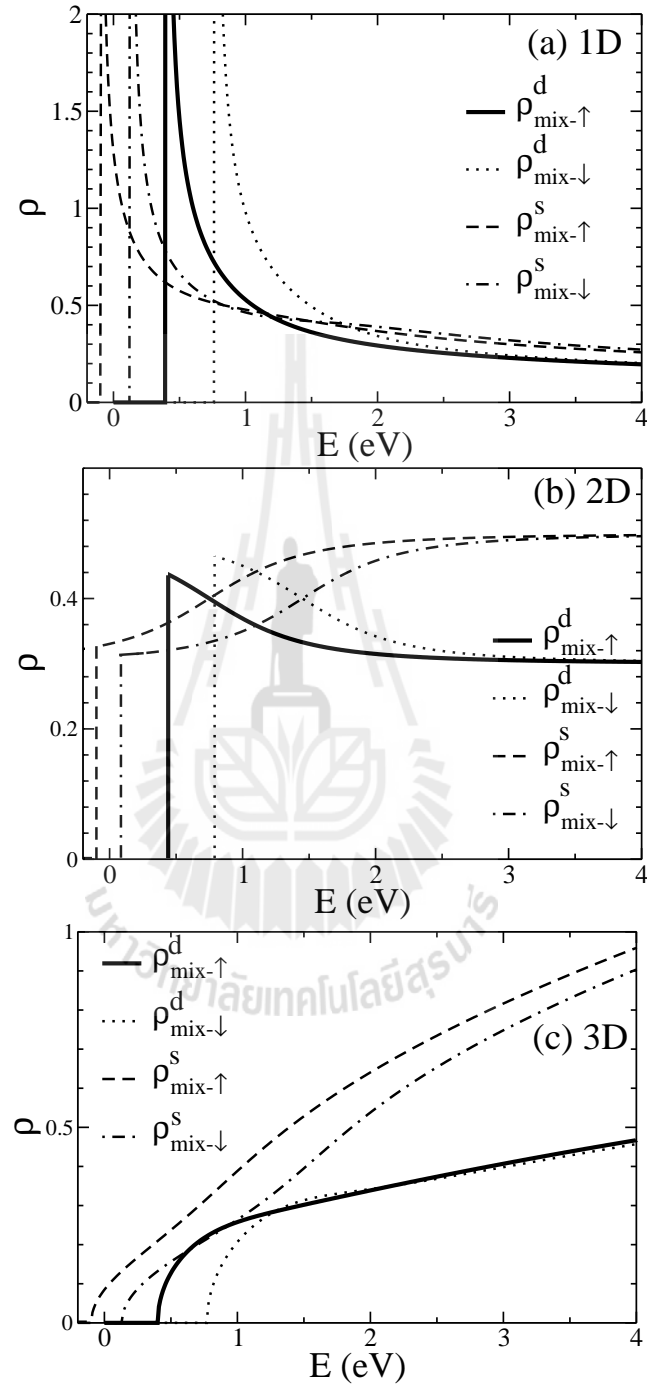
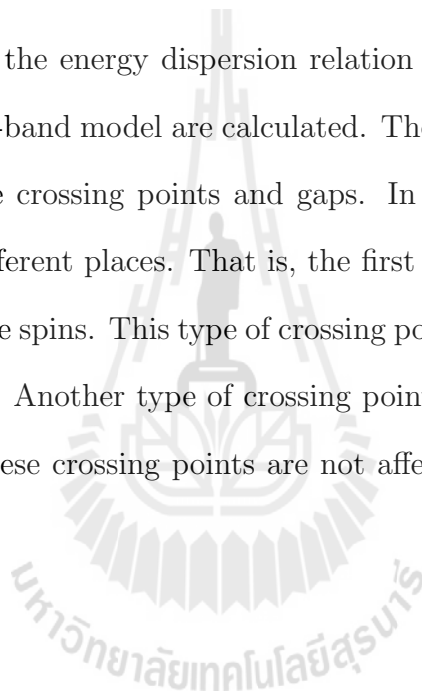


**Figure 3.7** The the DOS of two-bands ferromagnet are plotted for (a) 1D, (b) 2D, and (c) 3D systems. The exchange energies and the electron effective masses are the same as in Figure 3.4, but  $t = 0.2 \text{ eV}$ .

In Figures 3.5 - 3.7, the DOS of ferromagnet in 1D, 2D, and 3D system are shown in the two-band model when  $t$  is increased. The crossing points of the first kind open up as gaps. The gaps strongly depend on the coupling strength  $t$  as shown in Figure 3.7. Other than that, each energy band is either shifted up or shifted down due to the presence of the coupling strength  $t$ .

### 3.4 Conclusions

In this chapter, the energy dispersion relation and the density of states of a ferromagnet in the two-band model are calculated. There are two important physical features, which are the crossing points and gaps. In the first feature, the crossing points occur at two different places. That is, the first crossing points occur between the bands with the same spins. This type of crossing points is affected by the coupling strength tremendously. Another type of crossing point occurs between the bands of the opposite spins. These crossing points are not affected by the coupling strength as much.



# CHAPTER IV

## TUNNELING SPECTROSCOPY IN THE TWO-BAND APPROXIMATION

One of the powerful tools used to detect the electronic properties of a system is tunneling spectroscopy. In this Chapter, we will examine which features in the dispersion relation will show up in the conductance spectra.

### 4.1 The wave functions

The Hamiltonian of an M/FM junction is

$$\begin{aligned}
 H = & \hat{p} \frac{1}{m(x)} \hat{p} + \begin{bmatrix} E_0^d - E_{ex}^d & 0 & 0 & 0 \\ 0 & E_0^d + E_{ex}^d & 0 & 0 \\ 0 & 0 & E_0^s - E_{ex}^s & 0 \\ 0 & 0 & 0 & E_0^s + E_{ex}^s \end{bmatrix} \\
 & + U_0 \delta(x) - E_F \Theta(-x)
 \end{aligned} \tag{4.1}$$

where  $\hat{p}$  is momentum operator,  $U_0 = \begin{bmatrix} u_0 & 0 & 0 & 0 \\ 0 & u_0 & 0 & 0 \\ 0 & 0 & u_0 & 0 \\ 0 & 0 & 0 & u_0 \end{bmatrix}$ ,  $\delta(x)$  is the Dirac delta

function,  $E_0^{d(s)}$  is the off-set energy of the d(s) band in the ferromagnet,  $E_{ex}^{d(s)}$  is the exchange energy of spin-up (down) of the d (s) band, and  $E_F$  is Fermi energy in the metal (see Figure 4.1 for illustration), the position dependence of the electron

effective mass is (Zulicke and Schroll, 2001)

$$\frac{1}{m(x)} = \frac{1}{m_M^*} \Theta(-x) + \frac{1}{m_{FM}^{d(s)*}} \Theta(x), \quad (4.2)$$

where  $m_M^*$  is the electron effective mass in metal,  $\Theta$  is the Heaviside step function,  $m_{FM}^{d(s)*}$  is the electron effective mass of the d (s) band in the ferromagnet.

By solving eigenvalue problem, one can obtain the four corresponding of the eigenstates in a metal state;

$$\psi_{1\uparrow} = \begin{bmatrix} 1 \\ 0 \\ 0 \\ 0 \end{bmatrix} e^{iq \cdot r}; \quad \psi_{2\downarrow} = \begin{bmatrix} 0 \\ 1 \\ 0 \\ 0 \end{bmatrix} e^{iq \cdot r}; \quad \psi_{3\uparrow} = \begin{bmatrix} 0 \\ 0 \\ 1 \\ 0 \end{bmatrix} e^{iq \cdot r}; \quad \psi_{4\downarrow} = \begin{bmatrix} 0 \\ 0 \\ 0 \\ 1 \end{bmatrix} e^{iq \cdot r}, \quad (4.3)$$

where  $q = \sqrt{(E_k - E_F)2m_M^*/\hbar^2}$ .

In the ferromagnetic state, the four eigenstates are (see the detail how to obtain these eigenstates in Chapter III)

$$\psi_{\uparrow}^{\pm} = \frac{1}{N_{\uparrow}^{\pm}} \begin{bmatrix} -\left(\frac{\xi_{\uparrow}^d(k) - \xi_{\uparrow}^s(k) \mp \sqrt{|\xi_{\uparrow}^d(k) - \xi_{\uparrow}^s(k)|^2 + 4t^2}}{2t}\right) \\ 0 \\ 1 \\ 0 \end{bmatrix} e^{ik_{mix-\uparrow}^{d(s)} \cdot r}, \quad (4.4)$$

$$\psi_{\downarrow}^{\pm} = \frac{1}{N_{\downarrow}^{\pm}} \begin{bmatrix} 0 \\ -\left(\frac{\xi_{\downarrow}^d(k) - \xi_{\downarrow}^s(k) \mp \sqrt{|\xi_{\downarrow}^d(k) - \xi_{\downarrow}^s(k)|^2 + 4t^2}}{2t}\right) \\ 0 \\ 1 \end{bmatrix} e^{ik_{mix-\downarrow}^{d(s)} \cdot r}, \quad (4.5)$$

where  $N_{\sigma}^{\pm}$  are the corresponding normalization factors. The other parameters are already defined in Chapter III.

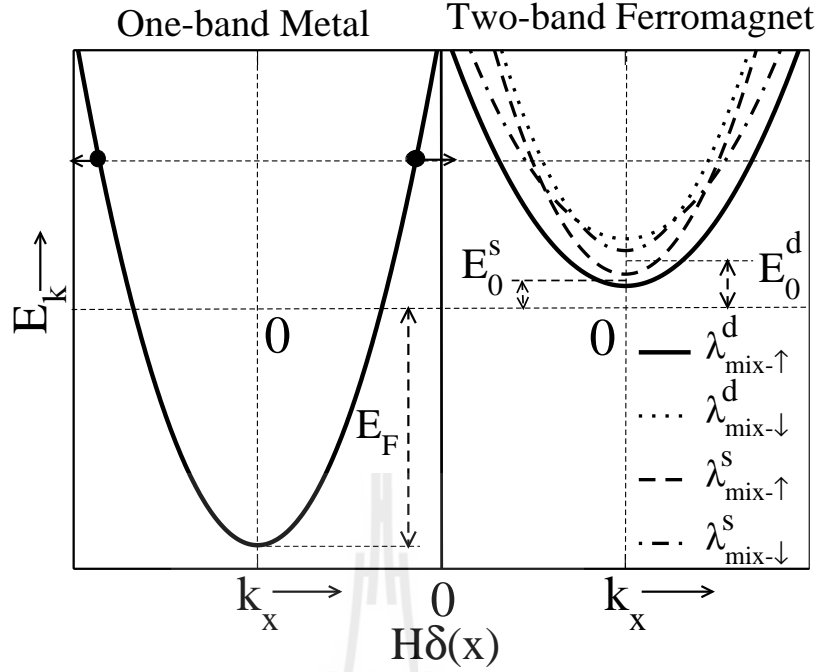


**Figure 4.1** Schematic illustration of the energy dispersion relation of one-band metal/two-band ferromagnet junction. The potential at the interface is defined by a delta potential  $U\delta(x)$ .  $E_F = 10E_{ex}^d$ ,  $t = 0.05 eV$ .

In this work, the energy dispersion relations of the electrons in the metal and the ferromagnet are illustrated in Figure 4.1. In this figure, the one-band metal is in the  $x < 0$  region while the two-band ferromagnet is in the  $x > 0$  region. For the injection of a given spin state from the metal side, the wave function of the quasiparticle in each region can be written as the linear combination of injected, and either reflected ( $r_{i,\sigma}$ ) or transmitted ( $t_{j,\sigma}$ ) states, where  $i$  refers to 1-4 states with spin  $\sigma$  in a metal side (see Equation 4.3 for illustration) while  $j$  refer to the four *mixed* states in ferromagnetic side. In this work, the scattering at the interface is considered to be a ballistic regime. There can be four equally possibly injected wave functions

in metal. There are

$$\Psi_M^{(1)}(\vec{r}) = \left( \begin{array}{c} \left[ \begin{array}{c} 1 \\ 0 \\ 0 \\ 0 \end{array} \right] e^{iq_x x} + \left[ \begin{array}{c} r_{1\uparrow}^{(1)} \\ 0 \\ r_{3\uparrow}^{(1)} \\ 0 \end{array} \right] e^{-iq_x x} \\ e^{i\vec{q}_{\parallel} \cdot \vec{r}_{\parallel}} \end{array} \right) \quad (4.6)$$

$$\Psi_M^{(2)}(\vec{r}) = \left( \begin{array}{c} \left[ \begin{array}{c} 0 \\ 0 \\ 1 \\ 0 \end{array} \right] e^{iq_x x} + \left[ \begin{array}{c} r_{1\uparrow}^{(2)} \\ 0 \\ r_{3\uparrow}^{(2)} \\ 0 \end{array} \right] e^{-iq_x x} \\ e^{i\vec{q}_{\parallel} \cdot \vec{r}_{\parallel}} \end{array} \right) \quad (4.7)$$

$$\Psi_M^{(3)}(\vec{r}) = \left( \begin{array}{c} \left[ \begin{array}{c} 0 \\ 1 \\ 0 \\ 0 \end{array} \right] e^{iq_x x} + \left[ \begin{array}{c} 0 \\ r_{2\downarrow}^{(3)} \\ 0 \\ r_{4\downarrow}^{(3)} \end{array} \right] e^{-iq_x x} \\ e^{i\vec{q}_{\parallel} \cdot \vec{r}_{\parallel}} \end{array} \right) \quad (4.8)$$

$$\Psi_M^{(4)}(\vec{r}) = \left( \begin{array}{c} \left[ \begin{array}{c} 0 \\ 0 \\ 0 \\ 1 \end{array} \right] e^{iq_x x} + \left[ \begin{array}{c} 0 \\ r_{2\downarrow}^{(4)} \\ 0 \\ r_{4\downarrow}^{(4)} \end{array} \right] e^{-iq_x x} \\ e^{i\vec{q}_{\parallel} \cdot \vec{r}_{\parallel}} \end{array} \right) \quad (4.9)$$

where  $\psi_M^{(l)}(\vec{r})$  refers to the total wave function of each injection process with spin-up ( $l = 1, 2$ ) and spin-down ( $l = 3, 4$ ) in metal.  $q_x = q = \sqrt{(2m_M^*/\hbar^2)(E + E_F)}$  in 1D system, where  $\vec{q}_{\parallel} = 0$  in 1D system,  $E_F$  is the Fermi energy in the metal, and  $m_M$  is its electron effective mass.  $\vec{r}_{\parallel}$  is a position vector along the line in 1D system. Here,  $r_{i,\sigma}^{(l)}$  is the amplitude of reflected electron with spin  $\sigma$  in metal state, where  $i = 1, 3$  refer to spin-up and  $i = 2, 4$  refer to spin-down components (see Equation 4.1 and Equation 4.3 for these indexes).

In the ferromagnetic side, the total wave function can also be written as a linear combination of transmission states. There are

$$\begin{aligned}
 \Psi_{FM}^{(l=1,2)}(\vec{r}) = & \left( \frac{t_{mix-\uparrow}^{(l)-d}}{N_{\uparrow}^+} \begin{bmatrix} -\left( \frac{\xi_{\uparrow}^d(k) - \xi_{\uparrow}^s(k) - \sqrt{|\xi_{\uparrow}^d(k) - \xi_{\uparrow}^s(k)|^2 + 4t^2}}{2t} \right) \\ 0 \\ 1 \\ 0 \end{bmatrix} e^{ik_{x-mix-\uparrow}^d x} \right. \\
 & + \left. \frac{t_{mix-\uparrow}^{(l)-s}}{N_{\uparrow}^-} \begin{bmatrix} -\left( \frac{\xi_{\uparrow}^d(k) - \xi_{\uparrow}^s(k) + \sqrt{|\xi_{\uparrow}^d(k) - \xi_{\uparrow}^s(k)|^2 + 4t^2}}{2t} \right) \\ 0 \\ 1 \\ 0 \end{bmatrix} e^{ik_{x-mix-\uparrow}^s x} \right) e^{i\vec{k}_{\parallel} \cdot \vec{r}_{\parallel}}
 \end{aligned} \tag{4.10}$$

for the case of injection electron with spin-up ( $l = 1, 2$ ) from metal, and

$$\begin{aligned}
 \Psi_{FM}^{(l=3,4)}(\vec{r}) = & \left( \frac{t_{mix-\downarrow}^{(l)-d}}{N_{\downarrow}^+} \begin{bmatrix} 0 \\ -\left( \frac{\xi_{\downarrow}^d(k) - \xi_{\downarrow}^s(k) - \sqrt{|\xi_{\downarrow}^d(k) - \xi_{\downarrow}^s(k)|^2 + 4t^2}}{2t} \right) \\ 0 \\ 1 \end{bmatrix} e^{ik_{x-mix-\downarrow}^d x} \right. \\
 & + \left. \frac{t_{mix-\downarrow}^{(l)-s}}{N_{\downarrow}^-} \begin{bmatrix} 0 \\ -\left( \frac{\xi_{\downarrow}^d(k) - \xi_{\downarrow}^s(k) + \sqrt{|\xi_{\downarrow}^d(k) - \xi_{\downarrow}^s(k)|^2 + 4t^2}}{2t} \right) \\ 0 \\ 1 \end{bmatrix} e^{ik_{x-mix-\downarrow}^s x} \right) e^{i\vec{k}_{\parallel} \cdot \vec{r}_{\parallel}}
 \end{aligned} \tag{4.11}$$

for the case of injection electron with spin-down ( $l = 3, 4$ ) from metal, where  $\xi_{\sigma}^{d(s)}$  are already defined in Equations 3.3 - 3.6 in previous chapter. Here,  $k_{x-mix-\sigma}^{d(s)} = k_{mix-\sigma}^{d(s)}$

in 1D system,  $k_{\parallel} = 0$  in 1D system. The expressions of these wave vectors are already defined in Equations 3.7 - 3.10 in Chapter III. The coefficients of the transmission as electron with spin-up in  $\lambda_{mix-\uparrow}^d$ -band and  $\lambda_{mix-\uparrow}^s$ -band in each injection ( $l$ ) process are respectively indicated by  $t_{mix-\uparrow}^d$  and  $t_{mix-\uparrow}^s$ . Also,  $t_{mix-\downarrow}^{(l)-d(s)}$  is the coefficient of the transmission state with spin-down in  $\lambda_{mix-\downarrow}^{d(s)}$ -band, corresponding to each injection ( $l$ ) process. All of the corresponding normalization factors are already defined in Chapter III.

#### 4.1.1 The matching conditions

The first matching condition is the continuity of the wave function at the interface;

$$\psi_M^{(l)}(x=0) = \psi_{FM}^{(l)}(x=0) = \psi_0^{(l)}, \quad (4.12)$$

where index  $l$  refers to each injection process from a metal side (see Equations 4.6 - 4.9 for illustration). The second matching condition is the discontinuity of the slope of the wave function due to the presence of the potential at the interface. That is,

$$\frac{m_M^*}{m_d^*} \frac{d\Psi_{FM}^{(l)}}{dx} \Big|_{0^+} - \frac{d\Psi_M^{(l)}}{dx} \Big|_{0^-} = 2k_F Z_0 \Psi_0^{(l)}, \quad (4.13)$$

for  $\lambda_{mix-\sigma}^d$  bands, and

$$\frac{m_M^*}{m_s^*} \frac{d\Psi_{FM}^{(l)}}{dx} \Big|_{0^+} - \frac{d\Psi_M^{(l)}}{dx} \Big|_{0^-} = 2k_F Z_0 \Psi_0^{(l)}. \quad (4.14)$$

for  $\lambda_{mix-\sigma}^s$ -bands, where a unitless parameter  $Z_0 = m_M^* u_0 / \hbar^2 q_F$ , and  $q_F$  is Fermi wave vector in metal. In this chapter, we neglect the spin-flip scattering at the interface because we have already known this effect on the transport properties in chapter II.

### 4.1.2 Reflection and transmission probabilities

We can calculate the reflection and transmission amplitudes,  $r_{i,\sigma}^{(l)}$ ,  $t_{mix-\sigma}^{(l)-d}$ ,  $t_{mix-\sigma}^{(l)-s}$ , from the matching conditions. From these amplitudes, one can obtain the corresponding probabilities. The definitions of the reflection and transmission probabilities  $R$  and  $T$  are (Shankar, 1994)

$$R = \frac{|J_{reflection}(x)|}{|J_{incident}|}, \quad (4.15)$$

$$T = \frac{|J_{transmission}(x)|}{|J_{incident}|}, \quad (4.16)$$

where  $J$  is the particle current density, which is equal to

$$J = \frac{i\hbar}{2m} \left[ \psi(x) \frac{d\psi^*(x)}{dx} - \psi^*(x) \frac{d\psi(x)}{dx} \right], \quad (4.17)$$

where  $m$  is quasiparticle mass, and  $\psi(x)$  is the wave function of the particle. After substitution of the corresponding  $\psi(x)$ , the following reflection and transmission probabilities can be obtained.

$$R_{i,\sigma}^{(l)} = |r_{i,\sigma}^{(l)}|^2, \quad (4.18)$$

$$T_{mix-\sigma}^{(l)-d} = |t_{mix-\sigma}^{(l)-d} \psi_{mix-\sigma}^{(l)-d}|^2 \frac{m_M k_{x-mix-\sigma}^d}{m_d q_x}, \quad (4.19)$$

$$T_{mix-\sigma}^{(l)-s} = |t_{mix-\sigma}^{(l)-s} \psi_{mix-\sigma}^{(l)-s}|^2 \frac{m_M k_{x-mix-\sigma}^s}{m_s q_x}, \quad (4.20)$$

where

$$\psi_{mix-\uparrow}^{d(s)} = \frac{-[\xi_{\uparrow}^d(k) - \xi_{\uparrow}^s(k) \mp \sqrt{|\xi_{\uparrow}^d(k) - \xi_{\uparrow}^s(k)|^2 + 4t^2}]}{2tN_{\uparrow}^{\pm}} \quad (4.21)$$

$$\psi_{mix-\downarrow}^{d(s)} = \frac{-[\xi_{\downarrow}^d(k) - \xi_{\downarrow}^s(k) \mp \sqrt{|\xi_{\downarrow}^d(k) - \xi_{\downarrow}^s(k)|^2 + 4t^2}]}{2tN_{\downarrow}^{\pm}} \quad (4.22)$$

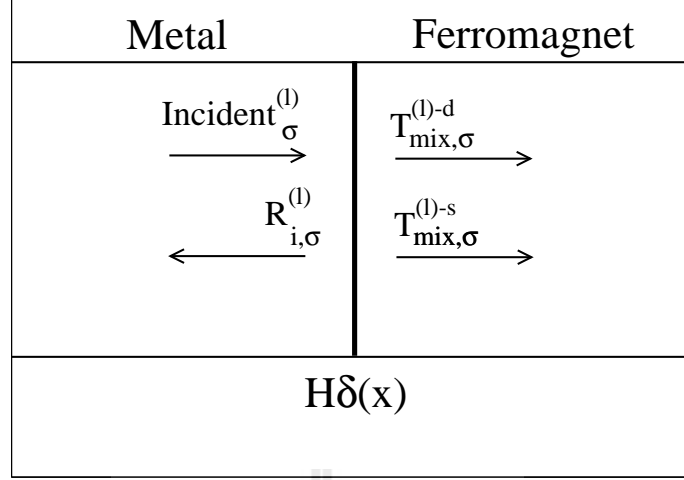


**Figure 4.2** The sketch of probabilities across the M/FM junction, where  $(l)$  refers to the four injection processes, and  $i$  refers to reflected as electron with spin-up ( $i = 1, 3$ ) and spin-down ( $i = 2, 4$ ).

We set the effective masses in spin-up and spin-down bands of electrons from the same band to be equal, i. e.  $m_{d\uparrow}^* = m_{d\downarrow}^*$  and  $m_{s\uparrow}^* = m_{s\downarrow}^*$ .

The total probability

$$R_{i,\sigma}^{(l)}(E) + T_{mix-\sigma}^{(l)-d}(E) + T_{mix-\sigma}^{(l)-s}(E) = 1, \quad (4.23)$$

where  $l$  refers to the four injection processes as explained in the text above. We use the probabilities to calculate the electric current density across the junction as will be discussed next.

## 4.2 Results and discussion

We now calculate the conductance spectra of the 1D M/FM junction  $G^{1D}$  using the two-band approach. We use a Landauer formula:

$$G_{\sigma}^{1D}(eV) = \frac{e^2}{h} [T_{mix-\sigma}], \quad (4.24)$$

where the total probability  $T_{mix-\sigma} = [T_{mix-\sigma}^{(1)-d(s)} + T_{mix-\sigma}^{(2)-d(s)} + T_{mix-\sigma}^{(3)-d(s)} + T_{mix-\sigma}^{(4)-d(s)}]/4$ .

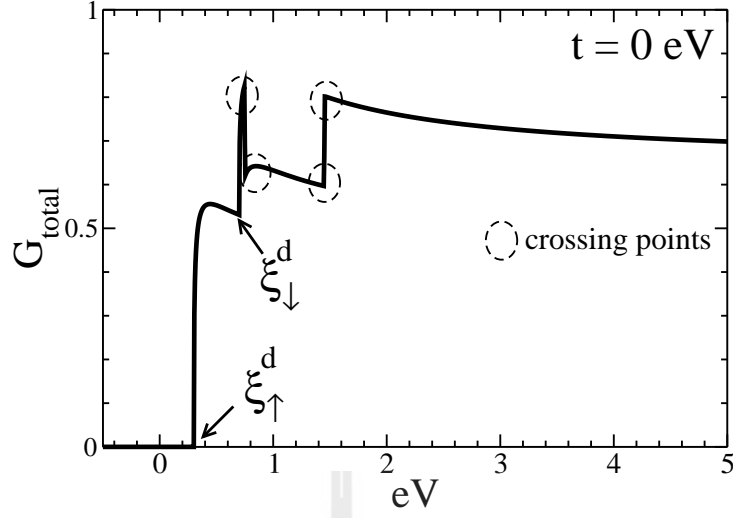


**Figure 4.3** Plot of the conductance spectra  $G$  as a function of energy  $E$ . Parameters are for  $Z_0 = 0$ ,  $E_{ex}^s = 0.1 eV$ ,  $E_{ex}^d = 0.2 eV$ ,  $E_0^s = 0.1 eV$ ,  $E_0^d = 0.5 eV$ ,  $m_M^* = 0.5m_e$ ,  $m_d^* = 0.5m_e$ ,  $m_s^* = 0.3m_e$ . The coupling strength  $t$  is zero. Solid arrows are indicated the bottom of each corresponding band.

The results are shown in Figure 4.3 - 4.6. In Figure 4.3, the conductance spectrum  $G$  in a case where the coupling strength  $t = 0$ . There are rich features occurring at the energy below the crossing point of the same spin band as indicated by dash circles. In this figure, the first and the second kinks indicated by arrows occur at the bottom of  $\xi_\sigma^d$  bands. Surprisingly, there is no any feature from  $\xi_\sigma^s$  bands.

As  $t$  increase, the conductance spectra are shown in Figure 4.4. In this figure, there are three important features. First, there are kinks at the bottom of  $\lambda_{mix-\sigma}^s$  bands and these kinks will be dominated with increasing  $t$ . Second, there still are kinks at the bottom of  $\lambda_{mix-\sigma}^d$  bands as also shown in Figure 4.3 where  $t = 0$ . Third, there are two peaks at the avoiding crossing points of the same spin band as indicated by dashed circles. In particular, the curve between these avoiding crossing points of this conductance spectrum is more smoothly with  $t$  increase. Eventually, these peaks will almost disappear with large  $t$  ( $t = 0.2 eV$ ). Interestingly, the conductance spectra in the large  $eV$  in the case where  $t$  is not zero behave like the one-band model. That is,  $G_{total}^{1D} \sim constant$  at large applied voltage  $eV$ . This behavior confirm that our expressions in two-band model are expected.

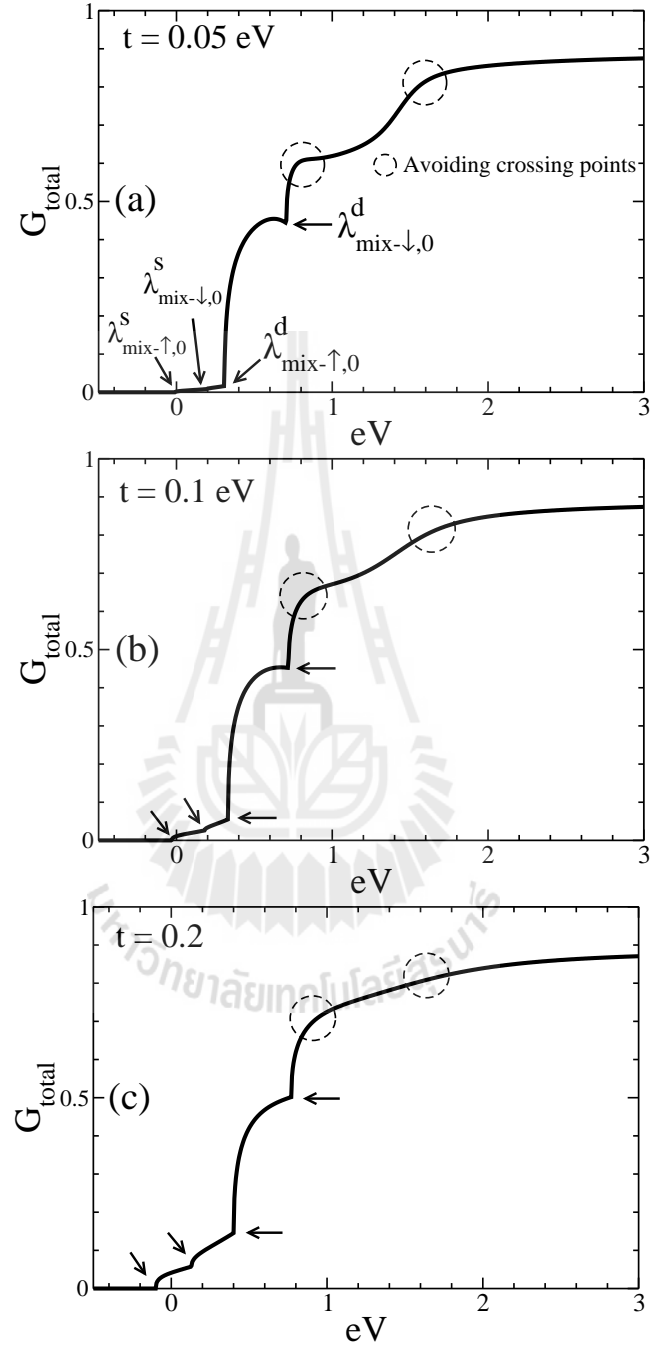


**Figure 4.4** Plots of the conductance spectra  $G$  as a function of energy  $E$ . Parameters are for  $Z_0 = 0$ ,  $E_0^s = 0.1$ ,  $E_0^d = 0.5$ ,  $E_{ex}^s = 0.1$ ,  $E_{ex}^d = 0.2$ ,  $m_M^* = 0.5m_e$ ,  $m_d^* = 0.5m_e$ ,  $m_s^* = 0.3m_e$ . In (a)  $t = 0.05$  eV, (b)  $t = 0.1$  eV, and (c)  $t = 0.2$  eV. Solid arrows are indicated the bottom of each corresponding band.

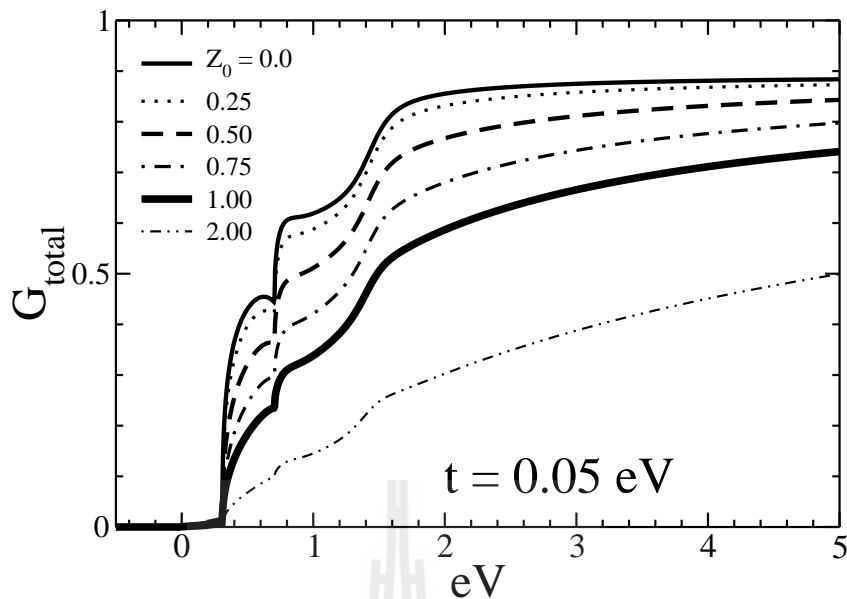


**Figure 4.5** Plots of the conductance spectra  $G$  as a function of applied biased voltage  $eV$  for various  $Z_0$ . The exchange energies and the electron effective masses are the same as in Figure 4.4, but  $t = 0.05 eV$ .

In two-band model, we also consider the effect of the interfacial non-spin-flip scattering  $Z_0$  at the interface on the conductance spectra. In Figure 4.5, the effect of  $Z_0$  on  $G$ , where  $t = 0.05 eV$ , is shown. It is found that the conductance spectra  $G$  decrease with increasing  $Z_0$ . This is an expected result, because we have already seen this feature in the one-band model. In this figure, the spectra in the metallic limit contain kinks at the bottom of the each band and the peaks at the avoiding crossing points. In the tunneling limit, these kinks and peaks are not as distinct and the conductance spectra look more smoothly. On the other words, the features predicted as the two-band model are most prominent in the metallic limit.

Because there are three electron effective masses,  $m_M^*$ ,  $m_s^*$ ,  $m_d^*$ , in this junction, we closely look into the effect of the electron effective mass on the conductance spectra  $G$  as shown in Figure 4.6. In this figure, the electron effective mass in metal  $m_M^*$  is varied but  $m_d^* = 0.5m_e$  and  $m_s^* = 0.3m_e$  stay the same. This plot is very interesting, because one can obtain an idea why many people model the Hamiltonian of ferromagnet by taking into account only the electrons from the d band. In Figure

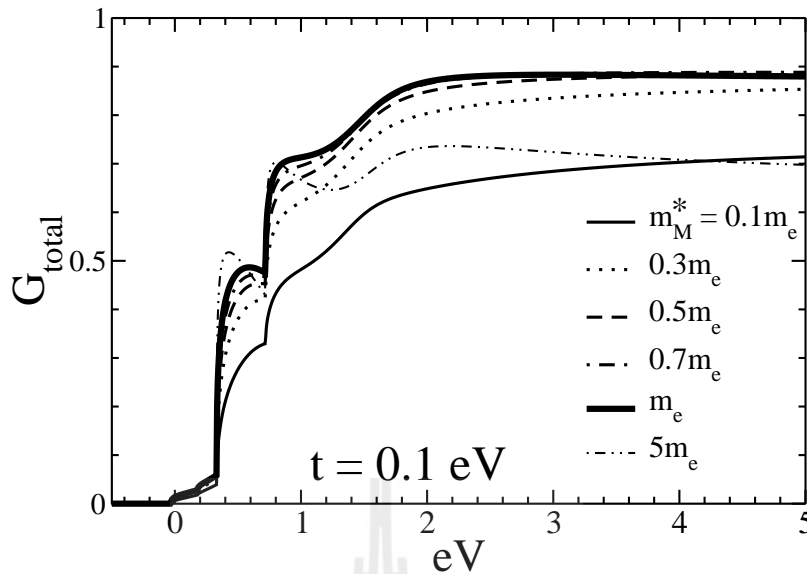


**Figure 4.6** Plot of the conductance spectra  $G$  as a function of biased voltage  $eV$  for various of the effective masses in metal  $m_M^*$ . Parameters are for  $Z_0 = 0.0$ ,  $E_0^s = 0.1 eV$ ,  $E_0^d = 0.5 eV$ ,  $E_{ex}^s = 0.1 eV$ ,  $E_{ex}^d = 0.2 eV$ . The electron effective masses in ferromagnet are  $m_d^* = 0.5m_e$ ,  $m_s^* = 0.3m_e$  fixed, where  $m_e$  is electron mass.

4.6, the increase  $G$  with increasing  $m_M^*$  until  $m_M^*$  is approximately equal to  $m_e$  can be seen. When  $m_M^*$  is larger than  $m_e$ ,  $G$  decrease. Also, the conductance is largest when  $m_M^*$  is very close to  $m_d^*$ . In this case, some electrons from metal can transmit into the s band. When  $m_M^*$  is larger than  $m_d^*$  ( $m_M^* \gg m_s^*$ ), the conductance  $G$  is increased because electrons can still transmit to the d band.

### 4.3 Conclusions

There are three important features occurring in the conductance spectra of the two-band model of a ferromagnetic material. There are only kinks at the bottom of the  $\lambda_{mix-\sigma}^d$  band when  $t = 0$ . When  $t$  is increased, the kinks at both the bottom of  $\lambda_{mix-\sigma}^s$  band and  $\lambda_{mix-\sigma}^d$  band are presented. The peaks in the conductance spectra at either the crossing points, when  $t = 0$ , or avoiding crossing points when  $t \neq 0$  are presented. These peaks are more prominent in the metallic limit than in the tunneling limit. Lastly, the conductance spectra are large, when the electron effective mass in the metal is a bit larger than that of the d band.

# CHAPTER V

## CONCLUSIONS

This thesis is a theoretical study the charge and spin transport in metal/ferromagnetic material junction using a scattering formalism. We consider both one-band and two-band approximations in describing the electronic properties of ferromagnetic materials.

In the one-band approximation, the main effects we have concentrated on is the dimensionality, the normal and spin-flip scattering at the interface. We found the following.

(i) There is a change of the slope of the conductance spectrum at the energy corresponding to the bottom of the minority band. This change occurs in all dimensional systems but it is most prominent in 1D system.

(ii) When the applied voltage is large, the conductance spectrum in all dimensional systems varies as  $G_{total}^{nD} \sim (eV)^{\frac{n-1}{2}}$ , where  $n$  is the dimensional number.

(iii) The conductance spectrum is suppressed, when the interfacial normal scattering strength is increased in the absence of the spin-flip scattering. When the spin-flip scattering is present, the conductance spectrum in the tunneling limit in all dimensional cases reaches the maximum value, when the normal scattering and non-spin-flip scattering strengths are equal.

(iv) The spin polarization of conductance is equal to one at the energy below the bottom of minority band, and is decreased when the energy is higher. This decrease is more rapid in 1D system than in 2D and 3D system.

(v) The spin polarization of conductance strongly depends on the dimensionality of the system. That is, in 1D system the spin polarization of conductance in a

metallic limit is increased with the spin-flip scattering strength to a maximum value. In the tunneling limit, the spin polarization of conductance is independent of the spin-flip scattering strength. In 2D and 3D system, the spin polarization of conductance is increased and reaches to a maximum value when the normal scattering and the spin-flip scattering strength are almost the same.

(vi) The spin polarizations of current in 1D, 2D, and 3D systems behave very similarly. That is, it can be enhanced to a maximum value when the normal scattering strength is equal to spin-flip scattering strength.

In the two-band model approximation, the s-d band mixing is included. The effect of the s-d coupling strength on the tunneling conductance spectrum of a ferromagnetic material is mainly considered. We have calculated the conductance spectrum  $G$  with varying the coupling strength  $t$ , and the electron effective masses. Our main findings are as follows.

(i) Because we have four energy dispersion relations, there are two kinds of the crossing points between bands, when the coupling strength  $t$  is equal to zero. They are the crossing points between the bands with the same spins and the crossing points between the bands with opposite spins. The first kind of the crossing points are opened as gaps when  $t$  is non-zero, while the second kind of the crossing points do not change much. The amplitudes of the gaps strongly depend on  $t$ .

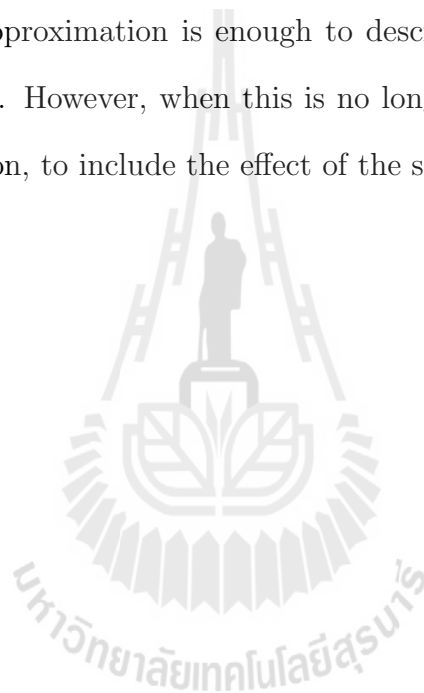
(ii) When  $t = 0$ , in the conductance spectrum in the low energy region, there are two kinks at the energies equivalent to the bottoms of the  $\lambda_{mix-\sigma}^d$  bands, but there are no features from the  $\lambda_{mix-\sigma}^s$  bands. In addition, there are two sharp peaks occurring at the energy corresponding to the crossing points between the bands with the same spin. In the higher energy region, the conductance spectrum behaves like that in the one-band model.

(iii) When  $t$  is presented, in the low energy region the four kinks still occur at the energies corresponding to the bottoms of the s-d mixing bands. The peaks at

the energy corresponding to the avoiding crossing points are also presented. In the higher energy region, the conductance spectrum still behaves like in the one-band model.

(iv) When the spin-flip scattering at the interface is not considered, the conductance spectrum is suppressed with the increasing normal scattering. This effect is similar to that in the one-band model.

(v) As long as, the effective mass in the metal is the same as that in the d band, the one-band approximation is enough to describe electronic properties of a ferromagnetic material. However, when this is no longer true, one needs to use the two-band approximation, to include the effect of the s band electrons.





## REFERENCES

## REFERENCES

- Ashcroft, N. W. and Mermin, N. D. (2003). **Solid State Physics**. Thomson Press.
- Baibich, M. N., Broto, J. M., Fert, A., Van Dau, F. N., Petroff, F., Etienne, P., Creuzet, G., Friederich, A., and Chazelas, J. (1988). Giant Magnetoresistance of (001)Fe/(001)Cr Magnetic Superlattices. **Phys. Rev. Lett.** 61(21): 2472–2475.
- Batallan, F., Rosenman, I., and Sommers, C. B. (1975). Band structure and Fermi surface of hcp ferromagnetic cobalt. **Phys. Rev. B** 11(1): 545–557.
- Binasch, G., Grunberg, P., Saurenbach, F., and Zinn, W. (1989). Enhanced magnetoresistance in layered magnetic structures with antiferromagnetic interlayer exchange. **Phys. Rev. B** 39(7): 4828–4830.
- Blonder, G. E. and Tinkham, M. (1983). Metallic to tunneling transition in Cu-Nb point contacts. **Phys. Rev. B** 27(1): 112–118.
- Božović, M. c. v. and Radović, Z. (2002). Coherent effects in double-barrier ferromagnet/superconductor/ferromagnet junctions. **Phys. Rev. B** 66(13): 134524.
- Callaway, J. and Wang, C. S. (1977). Energy bands in ferromagnetic iron. **Phys. Rev. B** 16(5): 2095–2105.
- Cullity, B. D. and Graham, C. D. (2008). **Introduction to Magnetic Materials**. Wiley-IEEE Press.
- de Jong, M. J. M. and Beenakker, C. W. J. (1995). Andreev Reflection in Ferromagnet-Superconductor Junctions. **Phys. Rev. Lett.** 74(9): 1657–1660.

- Dong, Z. C., Shen, R., Zheng, Z. M., Xing, D. Y., and Wang, Z. D. (2002). Quantum interference effects on tunneling conductance and shot noise in ferromagnet/ferromagnet/d-wave superconductor double tunnel junctions. **Phys. Rev. B** 65(21): 214512.
- Dong, Z. C., Shen, R., Zheng, Z. M., Xing, D. Y., and Wang, Z. D. (2003). Coherent quantum transport in ferromagnet/superconductor/ferromagnet structures. **Phys. Rev. B** 67(13): 134515.
- Fert, A. (2008). Nobel Lecture: Origin, development, and future of spintronics. **Rev. Mod. Phys.** 80(4): 1517–1530.
- Fert, A. and Jaffrès, H. (2001). Conditions for efficient spin injection from a ferromagnetic metal into a semiconductor. **Phys. Rev. B** 64(18): 184420.
- Filip, A. T., Hoving, B. H., Jedema, F. J., J. van Wees, B., Dutta, B., and Borghs, S. (2000). Experimental search for the electrical spin injection in a semiconductor. **Phys. Rev. B** 62(15): 9996–9999.
- Fujioka, K., Okamoto, J., Mizokawa, T., Fujimori, A., Hase, I., Abbate, M., Lin, H. J., Chen, C. T., Takeda, Y., and Takano, M. (1997). Electronic structure of SrRuO<sub>3</sub>. **Phys. Rev. B** 56(11): 6380–6383.
- Grunberg, P. A. (2008). Nobel Lecture: From spin waves to giant magnetoresistance and beyond. **Rev. Mod. Phys.** 80(4): 1531–1540.
- Guinea, F. (1998). Spin-flip scattering in magnetic junctions. **Phys. Rev. B** 58(14): 9212–9216.
- Žutić, I., Fabian, J., and Das Sarma, S. (2004). Spintronics: Fundamentals and applications. **Rev. Mod. Phys.** 76(2): 323–410.

- Jansen, R. and Moodera, J. S. (2000). Magnetoresistance in doped magnetic tunnel junctions: Effect of spin scattering and impurity-assisted transport. **Phys. Rev. B** 61(13): 9047–9050.
- Jedema, F. J., Nijboer, M. S., Filip, A. T., and van Wees, B. J. (2003). Spin injection and spin accumulation in all-metal mesoscopic spin valves. **Phys. Rev. B** 67(8): 085319.
- Kashiwaya, S., Tanaka, Y., Yoshida, N., and Beasley, M. R. (1999). Spin current in ferromagnet-insulator-superconductor junctions. **Phys. Rev. B** 60(5): 3572–3580.
- Kittel, C. (2005). **Introduction to Solid State Physics**. John Wiley and Sons: Inc.
- Kobayashi, M., Hwang, J. I., Song, G. S., Ooki, Y., Takizawa, M., Fujimori, A., Takeda, Y., Fujimori, S.-I., Terai, K., Okane, T., Saitoh, Y., Yamagami, H., Lin, Y.-H., and Nan, C.-W. (2008). Systematic changes of the electronic structure of the diluted ferromagnetic oxide Li-doped  $\text{Ni}_{1-x}\text{Fe}_x\text{O}$  with hole doping. **Phys. Rev. B** 78(15): 155322.
- Larsen, M. H., Lunde, A. M., and Flensberg, K. (2002). Conductance of Rashba spin-split systems with ferromagnetic contacts. **Phys. Rev. B** 66(3): 033304.
- Lyu, P., Xing, D. Y., and Dong, J. (1998). Tunneling magnetoresistance in mixed-valence manganite tunnel junctions. **Phys. Rev. B** 58(1): 54–57.
- Ma, M. J., Jalil, M. B. A., and Tan, S. G. (2009). Effect of interface spin-flip scattering on the spin polarized transport through a quantum dot: Master equation approach. **J. Appl. Phys.** 105(7): 07E907.
- Ma, M. J., Jalil, M. B. A., Tan, S. G., and Meng, H. Y. (2010). Spin-flip effects in

a ferromagnetic/normal-metal island/ferromagnetic double tunnel junction system. **J. Appl. Phys.** 107(11): 114321.

Marder, M. (2000). **Condensed Matter Physics**. New York: John Wiley and Sons.

Matsuyama, T., Hu, C.-M., Grundler, D., Meier, G., and Merkt, U. (2002). Ballistic spin transport and spin interference in ferromagnet/InAs(2DES)/ferromagnet devices. **Phys. Rev. B** 65(15): 155322.

Mijnarends, P. E. (1973). Position annihilation in 3d metals. **Physica**. 63(1): 235–247.

Nautiyal, T. and Auluck, S. (1985). Electronic structure of ferromagnetic iron: Fermi surface. **Phys. Rev. B** 32(10): 6424–6428.

Nautiyal, T. and Auluck, S. (1986). Electronic structure of ferromagnetic iron: Band structure and optical properties. **Phys. Rev. B** 34(4): 2299–2305.

Ngai, J. H., Atkinson, W. A., and Wei, J. Y. T. (2007). Tunneling Spectroscopy of *c*-Axis  $Y_{1-x}Ca_xBa_2Cu_3O_{7-\delta}$  Thin-Film Superconductors. **Phys. Rev. Lett.** 98(17): 177003.

Ohno, Y., Yong, D. K., Beschoten, B., Matsukura, F., Ohno, H., and Awschalom, D. D. (1999). Electrical spin injection in ferromagnetic semiconductor heterostructure. **Nature (London)** 431(16): 790–792.

Ohtori, H. and Imamura, H. (2009). Conductance oscillations due to geometrical resonance in FNS double junctions. **Phys. Rev. B** 79(21): 212507.

Okabayashi, J., Kimura, A., Rader, O., Mizokawa, T., Fujimori, A., Hayashi, T., and Tanaka, M. (2001). Angle-resolved photoemission study of  $Ga_{1-x}Mn_xAs$ . **Phys. Rev. B** 64(12): 125304.

- Pasanai, K. and Atkinson, W. A. (2010). Theory of (001) surface and bulk states in  $Y_{1-y}Ca_yBa_2Cu_3O_{7-\delta}$ . **Phys. Rev. B** 81(13): 134501.
- Pessa, M., Heimann, P., and Neddermeyer, H. (1975). Photoemission and electronic structure of iron. **Phys. Rev. B** 14(8): 3488–3493.
- Petrovykh, D. Y., Altmann, K. N., Hchst, H., Laubscher, M., Maat, S., Mankey, G. J., and Himpsel, F. J. (1998). Spin-dependent band structure, Fermi surface, and carrier lifetime of permalloy. **Appl. Phys. Lett.** 73(1): 3459–3462.
- Petrovykh, D. Y., Altmann, K. N., Hochst, H., Laubscher, M., Maat, S., and Mankey, G. J. (2007). Spin-dependent band structure, Fermi surface, and carrier lifetime of permalloy. **Appl. Phys. Lett.** 73(23): 3459–3461.
- Piper, L. F. J., DeMasi, A., Cho, S. W., Preston, A. R. H., Laverock, J., Smith, K. E., West, K. G., Lu, J. W., and Wolf, S. A. (2010). Soft x-ray spectroscopic study of the ferromagnetic insulator  $V_{0.82}Cr_{0.18}O_2$ . **Phys. Rev. B** 82(23): 235103.
- Pratt, W. P., Lee, S.-F., Slaughter, J. M., Loloee, R., Schroeder, P. A., and Bass, J. (1991). Perpendicular giant magnetoresistances of Ag/Co multilayers. **Phys. Rev. Lett.** 66(23): 3060–3063.
- Prinz, G. (1959). Spin-polarized transport. **Phys. Today** 48: 58–60.
- Rashba, E. I. (2000). Theory of electrical spin injection: Tunnel contacts as a solution of the conductivity mismatch problem. **Phys. Rev. B** 62(24): R16267–R16270.
- Schmidt, G., Ferrand, D., Molenkamp, L. W., Filip, A. T., and van Wees, B. J. (2000). Fundamental obstacle for electrical spin injection from a ferromagnetic metal into a diffusive semiconductor. **Phys. Rev. B** 62(8): R4790–R4793.

- Shankar, S. (1994). **Principle of Quantum Mechanics (2nd ed)**. Plenum Press: New York.
- Srisongmuang, B., Pairor, P., and Berciu, M. (2008). Tunneling conductance of a two-dimensional electron gas with Rashba spin-orbit coupling. **Phys. Rev. B** 78(15): 155317.
- Stoner, E. C. (1933). magnetic properties in ferromagnetic material. **Phil. Mag.** 15(1): 1018.
- Stoner, E. C. (1938). magnetic properties in ferromagnetic material. **Proc. R. Soc. Lond.** A165(1): 372.
- Taddei, F., Sanvito, S., Jefferson, J. H., and Lambert, C. J. (1999). Suppression of Giant Magnetoresistance by a Superconducting Contact. **Phys. Rev. Lett.** 82(24): 4938–4941.
- Tserkovnyak, Y., Brataas, A., and Bauer, G. E. W. (2002). Enhanced Gilbert Damping in Thin Ferromagnetic Films. **Phys. Rev. Lett.** 88(11): 117601.
- Turner, A. M., Donoho, A. W., and Erskine, J. L. (1984). Experimental bulk electronic properties of ferromagnetic iron. **Phys. Rev. B** 29(6): 2986–3000.
- van Son, P. C., van Kempen, H., and Wyder, P. (1987). Boundary Resistance of the Ferromagnetic-Nonferromagnetic Metal Interface. **Phys. Rev. Lett.** 58(21): 2271–2273.
- Vedyayev, A., Bagrets, D., Bagrets, A., and Diény, B. (2001). Resonant spin-dependent tunneling in spin-valve junctions in the presence of paramagnetic impurities. **Phys. Rev. B** 63(6): 064429.
- Wang, C. S. and Callaway, J. (1974). Band structure of nickel: Spin-orbit coupling,

the Fermi surface, and the optical conductivity. **Phys. Rev. B** 9(11): 4897–4907.

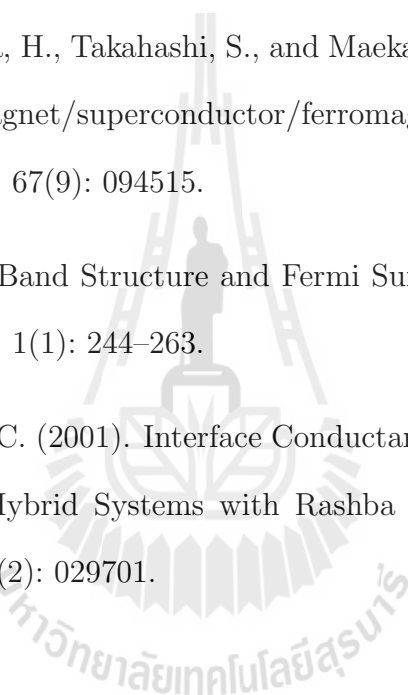
Wang, C. S. and Callaway, J. (1977). Energy bands in ferromagnetic nickel. **Phys. Rev. B** 15(1): 298–306.

Wang, S., Tang, L., and Xia, K. (2010). Spin transfer torque in the presence of Andreev reflections. **Phys. Rev. B** 81(9): 094404.

Yamashita, T., Imamura, H., Takahashi, S., and Maekawa, S. (2003). Andreev reflection in ferromagnet/superconductor/ferromagnet double junction systems. **Phys. Rev. B** 67(9): 094515.

Zornberg, E. I. (1970). Band Structure and Fermi Surface of Ferromagnetic Nickel. **Phys. Rev. B** 1(1): 244–263.

Zulicke, U. and Schroll, C. (2001). Interface Conductance of Ballistic Ferromagnetic-Metal-2DEG Hybrid Systems with Rashba Spin-Orbit Coupling. **Phys. Rev. Lett.** 88(2): 029701.



# CURRICULUM VITAE

**NAME** Mr. Krisakron Pasanai  
**DATE OF BIRTH** June 29, 1981  
**PLACE OF BIRTH** Mahasarakham, Thailand  
**PERSONAL ADDRESS** 141, Nonghai, Wapeepathum,  
Mahasarakham 44120, Thailand  
Tel. -, Mobile. 66-088-3079409  
**E-MAIL** krisakron\_Lak@hotmail.com

## EDUCATION

PhD candidate (2005 - 2011)

School of Physics, Suranaree University of Technology, Nakhon Ratchasima,  
Thailand

Title of Thesis: CHARGE AND SPIN TRANSPORT OF FERROMAGNETIC  
MATERIALS

Supervisor: Assoc. Prof. Dr. Puangratana Pairor

Bachelor of Science (2004)

Department of Physics, Mahasarakham University, Mahasarakham, Thailand

Supervisor: Mr. Pisanu Punjarernsil